Strong variability in the thermal structure of Tibetan Lithosphere

B. Xia [1*], I.M. Artemieva [2,3,4.5*], H. Thybo [4,5,6], S.L. Klemperer [2]

[1] State Key Laboratory of Lithospheric Evolution, Institute of Geology and Geophysics, Chinese Academy of Sciences, Beijing, China

[2] Department of Geophysics, Stanford University, 397 Panama Mall, Stanford, CA 94305, USA

[3] Section of Marine Dynamics, GEOMAR Helmholtz Center for Ocean Research, Wischhofstr. 1-3, Kiel 24148, Germany

[4] SinoProbe Laboratory, Chinese Academy of Geological Sciences, Beijing,China

[5] State Key Laboratory of Geological Processes and Mineral Resources, School of Earth Sciences, China University of Geosciences, No. 388 Lumo Road, Wuhan 430074, China

[6] Eurasia Institute of Earth Sciences, Istanbul Technical University, Maslak, Istanbul, Turkey

*Corresponding authors:

B. Xia: bingxia0127@gmail.com,

I.M.Artemieva: iartemieva@gmail.com

Key Points:

- Thick Tibetan lithosphere defines the longitudinally variable northern extent of the Indian plate.
- The 'North Tibet Anomaly' with a hot mantle marks the junction of the Indian and Asian slabs.
- Tethyan paleo-slabs explain variable lithosphere thickness in eastern Tibet.

This article has been accepted for publication and undergone full peer review but has not been through the copyediting, typesetting, pagination and proofreading process, which may lead to differences between this version and the Version of Record. Please cite this article as doi: 10.1029/2022JB026213.

Abstract

We present a model of thermal lithospheric thickness (the depth where the geotherm reaches a temperature of 1300°C) and surface heat flow in Tibet and adjacent regions based on a new thermal-isostasy method. The method accounts for crustal density heterogeneity, is free from any assumption of a steady-state lithosphere thermal regime, and assumes that deviations from crustal Airy-type isostasy are caused by lithosphere thermal heterogeneity. We observe a highly variable lithospheric thermal structure which we interpret as representing longitudinal variations in the northern extent of the subducting Indian plate, southward subduction of the Asian plate beneath central Tibet, and possible preservation of fragmented Tethyan paleo-slabs. Cratonic-type cold and thick lithosphere (200-240 km) with a predicted surface heat flow of 40-50 mW/m^2 typifies the Tarim Craton, the northwest Yangtze Craton, and most of the Lhasa Block that is likely refrigerated by underthrusting Indian lithosphere. We identify a 'North Tibet anomaly' with thin (<80 km) lithosphere and high surface heat flow (>80-100 mW/m^2). We interpret this anomaly as the result of removal of lithospheric mantle and asthenospheric upwelling at the junction of the Indian and Asian slabs with opposite subduction polarities. Other parts of Tibet typically have intermediate lithosphere thickness of 120-160 km and a surface heat flow of 45-60 mW/m^2, with patchy anomalies in eastern Tibet. While different uplift mechanisms for Tibet predict different lithospheric thermal regimes, our results in terms of a highly variable thermal structure beneath Tibet suggest that topographic uplift is caused by an interplay of several mechanisms.

Plain Language Summary

The world's highest and largest plateau in Tibet has a unique topography with an average elevation of >4 km and is often named "the Roof of the world". Continental collision between the Indian and Eurasian plates created Tibet and the Himalaya, and the dynamics of plateau growth and related large-scale regional geological processes present a series of intriguing geoscience problems. Several geodynamic models involving modification of the entire lithosphere have been proposed as mechanisms for the Tibetan uplift. Two end-member models involve either a "cold" or a "hot" Tibetan lithosphere. As different uplift mechanisms predict different lithospheric thermal regimes, knowledge of the thermal structure is key to understanding the driving forces of the Tibetan uplift. However, the thermal regime of Tibet is poorly known from surface heat-flow measurements as high-quality observations are almost absent. To bypass the problem of limited geophysical data coverage, we use a new thermal isostasy method to constrain the lithospheric thermal structure of Tibet and adjacent areas. Our results show a strongly variable lithospheric thermal structure beneath Tibet and suggest that topographic uplift is caused by an interplay of several mechanisms.

1 Introduction

Continental collision between the Indian and Eurasian Plates created the high Tibet Plateau and the Himalayas (Figure 1a). The dynamics of plateau growth and related large-scale regional geological processes operating during orogenesis present a series of intriguing geoscience problems (England and Houseman, 1988; Klemperer, 2006; Tapponnier et al., 2001; Yin and Harrison, 2000; Hou et al., 2004, Li and Song., 2018). Several geodynamic models involving modification of the entire lithosphere have been proposed as mechanisms for the Tibetan uplift. The end-member models involve either a “cold” or a “hot” Tibetan lithosphere: while plateau uplift caused by successive terrane collision/accretion events suggests a rigid and cold lithosphere (Tapponnier et al., 2001), continuous thickening of the lithosphere followed by its partial or complete removal and upwelling of asthenosphere material results in a hot Tibetan lithosphere (England and Houseman, 1988). Recent geological and seismic studies indicate that the subducting Indian plate may be fragmented (Hou et al., 2004, Li and Song., 2018), which forms hot, thin lithosphere around slab windows of asthenosphere upwelling, and maintains cold, thick lithosphere where the subducting slab is intact.

As different uplift mechanisms predict different lithospheric thermal regimes, knowledge of the thermal structure is key to understanding the driving forces of the Tibetan uplift. However, the thermal regime of Tibet is poorly known from surface heat-flow measurements as high-quality (class A and B with depth of measurement >300 m) observations are almost absent and are largely limited to the Eastern Kunlun-Qaidam Block in northern Tibet (Figure 1b and Supporting

Figure S1; Jiang et al., 2019). The few existing heat-flow measurements in inner Tibet are along roads that usually follow major faults and, therefore, may be severely affected by groundwater circulation; and further most of the measurements in inner Tibet were made at depths of <10 meters and in areas with hot springs (e.g. Francheteau et al., 1984; Supporting Figure S1). Therefore, the heat-flow measurements in Tibet have much larger uncertainties than the typical value of 10-15% on continents (Jaupart and Mareschal, 2011). The true uncertainty cannot be assessed because of the non-steady state thermal regime affecting borehole measurements, which is often the case in industrial wells, either due to groundwater circulation or to non-equilibrium temperatures due to drilling.

Despite international efforts, the lithospheric thermal structure of Tibet is largely unconstrained in most of the region (Figure 1b) due to extremely complicated logistics for data acquisition, while global thermal models (e.g. Artemieva, 2006; McKenzie and Priestley, 2008) have low resolution and can resolve only major features of the lithospheric thermal structure (e.g. Supporting Figure S2). To bypass the problem of limited geophysical data coverage, we use the new thermal isostasy method (Artemieva, 2019a,b, 2022; Artemieva and Shulgin, 2019) to constrain the lithospheric thermal structure of Tibet and adjacent areas from 74-110^{o} E and 26-42^{o} N. The method requires knowledge of topography, which is available globally in high resolution, and Moho depth, which we have compiled from published regional seismic studies (see section 4.3 and Figure 2).

In this study our interpretations of lithospheric thickness always refer to "thermal lithosphere", i.e., the layer characterized by conductive heat transport

above the asthenospheric mantle with a designated potential temperature, here 1300°C (e.g. Artemieva, 2006). We use the terms “thick” and “thin” thermal lithosphere, while recognizing that, by definition, our thick lithosphere is always colder than thin lithosphere at the same depth (Pollack et al., 1993; Rudnick et al., 1998). In contrast, xenolith and seismic-velocity interpretations reported here refer to temperature (or temperature contrasts), and therefore are described in terms of “hot” and “cold” lithosphere.

In the following we first provide an overview of the geology and tectonics of Tibet, details of previous studies of the thermal lithosphere structure of Tibet, and the geophysical data used in this study. This is followed by a short description of the methodology applied and results with sensitivity analysis. Finally, we present a discussion of the resulting heterogeneous thermal lithosphere structure and conclusions.

2 Geological and tectonic background

The Himalayan - Tibetan Plateau (Figure 1a) of the eastern Tethys tectonic belt includes from south to north the Himalayan orogenic belt, the Lhasa Block, the Qiangtang Block, the Songpan-Ganzi Block, the Eastern Kunlun-Qaidam Block, and the Qilian Block. These tectonic blocks are separated by major faults and sutures that possibly extend to the base of the lithosphere. The Himalayan - Tibetan Plateau region continues westward in the Tethyan Belt and is otherwise bordered by (Figure 1a):

- the Tarim Craton (2.5 - 0.8 Ga (Zhao et al., 2013) and possibly older (Ge et al., 2018)) in the north at the Altyn-Tagh strike-slip Fault (ATF),
- the North China Craton (3.8 – 2.5 Ga, Zhao et al., 2013) in the northeast at the North Qinling strike-slip Fault (NQF),
- the Yangtze Craton (3.5 - 2.5 Ga; Zhao et al., 2013 and references therein) in the east at the Longmenshan strike-slip Fault (LMF),
    - and the Indian Plate (>1.8 Ga; Chardon et al., 2008) in the south at the Main Boundary Thrust (MBT) at the southern edge of the Himalayas.

The formation of Tibet records the closure of the Tethys oceans since the early Paleozoic and particularly the collision between the Indian and Eurasian Plates since ~55 Ma (Yin and Harrison, 2000). The northern part of Tibet (the Eastern Kunlun-Qaidam and Qilian Blocks) consists of early Paleozoic blocks that record the closure of the Paleo-Tethys Ocean.

The Songpan-Ganzi Block, the Qiangtang Block, and the Lhasa Block were assembled during the closure of the Paleo-Tethys Ocean in Mesozoic time (Roger et al., 2010). The triangular Songpan-Ganzi Block is interpreted as a Middle to Late Triassic (230-200 Ma) basin. The northern Qiangtang Block is characterized by widespread 8-0 Ma volcanism with several occurrences of deep-seated crustal xenoliths (Ding et al., 2007; Hacker et al., 2000).

Detailed geochemical studies of volcanic rocks and granites indicate different tectonic origins for the southern and northern Lhasa Block, with an unusual crustal block in the middle Lhasa terrane (Wang et al., 2021). Neoproterozoic basement

has been found in the eastern Lhasa Block (Zhu et al., 2013) but not in the western Lhasa Block, which is characterized by widespread 25-8 Ma volcanism (Guo and Wilson, 2019). In the southern Lhasa Block, high-pressure metamorphic rocks (in eclogite facies) mark the closure of the Neo-Tethys Ocean.

The Himalayan belt formed by collision between the Indian and Eurasian plates at 55-0 Ma. It is composed of thick sediments from the Neo-Tethys Ocean, which are intruded by Cenozoic granites, above the Neoproterozoic basement (Zhu et al., 2013).

3 Previous geophysical and geochemical interpretations of the Tibetan thermal regime

The thermal structure of Tibetan lithosphere has been analysed in several geophysical experiments, illustrated in Figure 1b and detailed in Table 1. Seismic studies in north-central Tibet (No. 1 in Figure 1b) show low Pn velocity and a zone with inefficient Sn propagation which suggests a relatively high sub-Moho temperature (Ni and Barazangi, 1983; McNamara et al., 1997). Seismic and MT studies constrain lithospheric temperature along the INDEPTH III profile (Nos. 2-5 in Figure 1b) and along SW-NE trending profiles (Nos. 6-12 in Figure 1b).

Several studies along the INDEPTH III profile indicate that the central Lhasa Block has mostly cold lithosphere, with a sharp transition to a hot lithosphere in the Qiangtang Block. An integrated geophysical-petrological analysis based on electromagnetic and seismic data along the INDEPTH III profile (No. 4 in Figure

1b) suggests that the surface heat flow is up to 80 mW/m^2 in the Qiangtang Block in central Tibet and down to 65 mW/m^2 in the central Lhasa Block (Vozar et al., 2014). Similarly, seismic tomography (profile No. 2 in Figure 1b) shows that the lithosphere is >300 km thick (and therefore cold) in the central Lhasa Block and <100 km (and therefore hot) in the Qiangtang Block (Tilmann, 2003) in the same region where crustal xenoliths also indicate high crustal temperatures (Nos. 13-14 in Figure 1b). Earthquake thermometry along the same profile (No. 5 in Figure 1b) indicates a relatively cold lithosphere down to 200 km depth in the Lhasa Block and thin lithosphere (<80 km thick) beneath the Qiangtang Block (Wang et al., 2013). In contrast, an estimate based on the α−β quartz transition (No. 3 in Figure 1b) indicates a temperature of 700 °C in the upper-middle crust (depth of 20-40 km) of the central Lhasa Block (Mechie et al., 2004) and thus implies a lithosphere thickness of less than 100 km for an equilibrium geotherm.

A number of seismic, MT and gravity studies along a SW–NE trending profile from the Indian plate in the south towards the North China Craton in the north (Nos. 6-9 in Figure 1b, Table 1) provide constraints on the lithospheric thermal structure in several tectonic blocks of central-eastern Tibet. P-wave tomography (No. 6 in Figure 1b) suggests the presence of a cold lithosphere beneath the eastern Lhasa Block, a hot lithosphere below the eastern Qiangtang Block, and an intermediate ("warm") thermal regime at the NE end of the profile (Liang et al., 2012). Similarly, a gravity study (No. 7 in Figure 1b) indicates a very thick (>300 km) lithosphere in the eastern Lhasa Block, a thin (120 km) and hot lithosphere in the central part of the profile beneath the Qiangtang Block, and an intermediate lithosphere thickness

(~160 km) in the north (the Qaidam and Songpan-Ganzi Blocks) (Jiménez-Munt et al., 2008). These results are consistent with an S-receiver function study (No. 8 in Figure 1b) which concludes that the lithosphere is 180 - 220 km thick in the eastern Lhasa Block, ~100 km thick in the eastern Qiangtang Block and 120-160 km thick in the central Songpan-Ganzi Block (Zhao et al., 2011). Similarly, a magnetotelluric study (No. 9 in Figure 1b) indicates that the Qiangtang and Songpan-Ganzi Blocks in the central part of the profile have hot lithosphere and that the lithosphere of the eastern Lhasa Block is cold (Unsworth et al., 2004; Wei et al., 2001).

In eastern Tibet, joint interpretation of seismic Vp, Vs and attenuation along a ca. 400 km long profile (No. 10 in Figure 1b) indicates huge temperature variations in the lower crust (at a depth of 40–70 km) from 900 °C in the northern Qiangtang Block to 500 °C in the Songpan-Ganzi Block (Galvé et al., 2006). In western Tibet (No. 11 in Figure 1b), earthquakes deeper than 50 km which implies that Indian crust underthrusts northwestern Tibet close to the Tarim Craton (Wang and Klemperer, 2021). A similar study in south-central Tibet (No. 12 in Figure 1b) reports contrasting thermal regimes with the transition between a cold subducting Indian lithosphere in the south and a hot thin lithosphere in the central Qiangtang Block located around the Bangong–Nujiang suture (Craig et al., 2020).

Geochemical studies of crustal xenoliths in ~3 Ma volcanics (No. 13 in Figure 1b, Table 1) show that the crust of northern Tibet (the central Qiangtang Block) is very hot with temperatures of up to 800–1100 °C at a depth of 30-50 km (Hacker et al., 2000) in an area, where geophysical studies also indicate the presence of hot lithosphere. Similarly, crustal xenoliths from southernmost Qiangtang indicate

temperatures of >980-1080 °C at depths <50 km at 28 Ma (Ding et al., 2007; No. 14 in Figure 1b), and in the western Lhasa Block (No. 15 in Figure 1b) ~17 Ma mantle xenoliths constrain the middle Miocene temperatures of 1050-1250 °C at 50–65 km depth (Liu et al., 2011). These three sites all indicate an unusually hot, moderately thickened crust with temperatures reaching 1000 - 1100 °C at the Moho at less than ca. 60 km depth.

In contrast, crustal xenoliths brought to the surface in western Lhasa Block close to the Yarlung Zangbo suture zone at 13 Ma (No. 16 in Figure 1b) indicate a much cooler crust with temperatures of only 750–900 °C at 50–60 km depth and <~1300 °C at the ~80 km deep Moho (Chan et al., 2009). These results are in overall agreement with seismic receiver-function results and seismicity along the Yarlung Zangbo suture zone (ca. 29.5° N, 88-92° E; Shi et al., 2020).

Overall, all geophysical and xenolith-based models of the thermal structure of the Tibetan lithosphere are convincingly consistent. They show the presence of a cold and thick lithosphere in the entire Lhasa Block, an intermediate lithosphere thickness and temperature regime in north-eastern Tibet, and the presence of an anomalously hot and thin lithosphere in north-central Tibet (Figure 1b).

4 Geophysical data

4.1 Free-air gravity anomalies

For our analysis it is important that the study region is close to isostatic equilibrium. Free-air gravity anomalies (based on the high-resolution EGM2008

model on a 5′ × 5′ grid, Pavlis et al., 2012) are within ±50 mGal in most of Tibet and the adjacent regions (the west-central Tarim and North China Cratons) (Figure 1c), which suggests general near-isostatic equilibrium in most of the study area. The Yangtze Craton is also close to isostatic equilibrium with free-air gravity anomalies typically around -50 to -70 mGal, except for the narrow belt at the western edge with anomalies of ca. -75 to -120 mGal.

Within the Tibetan Plateau, only the Eastern Kunlun Block is not in isostatic equilibrium with relatively strong negative free-air anomalies of -50 to -120 mGal. Otherwise major deviations from isostasy (possibly caused by lithosphere flexure) occur mostly along its actively deforming margins. A positive free-air gravity anomaly of up to +200 mGal is observed in the Himalaya and southeastern Tibet (south of 30 ºN in the Lhasa and Songpan-Ganzi Blocks), with a strong negative free-air gravity anomaly of -100 mGal to -200 mGal further south at the northern margin of Indian Plate.

The Tarim craton is close to isostatic equilibrium in its western-central part (+20 to -80 mGal), and deviates from isostasy in the north-eastern part (-75 to -100 mGal). Besides, the northern boundary of Tibet at the Tarim Craton is also in disequilibrium with a narrow (<100 km wide) anomaly of ca. +120 mGal (locally ca. +200 mGal) on the Tibetan side and -120 to -150 mGal on the Tarim side. This characteristic pattern of positive and negative free-air gravity anomaly belts (cf. Artemieva et al., 2016) indicates the presence of a south-dipping subducting slab below the Altyn Tagh fault, as also inferred from some geochemical (Guo and Wilson, 2019) and geophysical (Zhao et al., 2011) data. A similar pattern is

observed at the Himalayan front with its north-dipping subduction.

4.2 Surface heat-flow measurements

We summarize here information on conventional borehole heat-flow measurements, which we further use to compare the predicted heat flow with observations. Surface heat-flow measurements are almost absent in Tibet, except in the petroliferous Qaidam sedimentary basin (Figure 1b; Jiang et al., 2019). In the Eastern Kunlun-Qaidam Block, surface heat-flow ranges from 40 mW/m^2 to 70 mW/m^2 with an average of 58±9 mW/m^2. Along the INDEPTH II profile, surface heat flow measured close to hot springs (see Supporting Figure S1b) shows high values up to 100-140 mW/m^2. However, these shallow measurements are of relatively low quality, and are probably significantly affected by groundwater circulation.

In the Tarim Craton, surface heat-flow measurements are concentrated in the north, while most of the central and southern parts have few measurements. The average value of surface heat flow is 42±3 mW/m^2 which corresponds to a typical Precambrian lithosphere (Artemieva, 2006). The adjacent North China and Yangtze Cratons have good coverage by surface heat-flow measurements of variable quality (dots in Figure 1b show only high-quality data, all heat flow measurements are shown in Supporting Figure S1). Compared to typical Archean lithosphere, surface heat flow is relatively high in the western North China Craton (with values of 64±10 mW/m^2 on average), possibly because of its post-Mesosoic reworking (Xia et al., 2020 and references therein). In the north-western Yangtze Craton, surface heat flow ranges from 40 mW/m^2 to 65 mW/m^2 with an average of

58±5 mW/m^2, and most measurements are in the western part.

On the whole, reliable heat-flow data are absent for most of Tibet, and the existing high-quality data are within the ranges expected for a thick and cold cratonic lithosphere. Note that no high-quality heat-flow measurements exist at the locations of geophysical profiles (Figure 1b).

4.3 Moho depth

Our calculations require information on the Moho depth, which we review in brief here. The Moho depth in Tibet is constrained by seismic studies (Figure 2a) which include both classic reflection/refraction profiles and receiver function (RF) results (see Table 2 for references). In northeastern Tibet, the Yangtze Craton, and the North China Craton, the Moho depth constrained by RF studies and refraction profiles differs by <5 km (Figure 2d). In these provinces, the crust is thick (>50 km in most regions), and therefore the uncertainty of <5 km is within <10% error and is acceptable for our calculations (see Table 3 for sensitivity analysis).

However, in many parts of Tibet, the difference in the Moho depth between results based on seismic reflection/refraction profiles and receiver function (RF) studies is relatively large (Figure 2d). In southern Tibet and the Tarim Craton, there are local >15 km differences in the Moho depth between the two methods. In the Lhasa and Qiangtang Blocks, the crust is >60 km thick (Figure 2c), and most refraction profiles in this region are ca. 400-500 km long which is too short to properly study the >60 km deep Moho (Figure 2a; Zhang et al., 2011 and references therein), except for one profile in the Central part of the Lhasa Block (Wang et al., 2021). We therefore use only RF results for the Moho depth, also

because they have a denser coverage.

The Moho depth is highly variable in Tibet and adjacent regions with values ranging from 36 to 80 km locally (Figure 2b and references in Table 2). The Himalayan belt, which has the highest elevations in the world (on average >6 km), has a Moho depth of 40 to 50 km. The Moho is deepest (65 km–80 depth) in the Lhasa Block (e.g. Shi et al., 2020) and >60 km in the Qiangtang Block. The Moho in the Songpan-Ganzi Block is deep (60-70 km depth) in the east and shallower (50-60 km depth) in the west. The Eastern Kunlun - Qaidam Block has the shallowest Moho in Tibet with values of 40 - 56 km. Beneath the Qilian Block the Moho is 55-60 km deep and regionally reaches 60–65 km depth. The adjacent Precambrian Yangtze, North China and Tarim Cratons have Moho at 35 - 45 km depth, similar to the Indian Plate.

5 Method and model parameters

5.1 Method overview

Our calculation of the lithospheric thermal structure is based on the thermal-isostasy method (Artemieva, 2019a, b, 2022), further detailed and tested by Artemieva and Shulgin (2019). It allows for calculation of the thickness of the thermal lithosphere, lithospheric mantle geotherms (not calculated here), and surface heat flow, which can be tested against borehole measurements. In particular, the method was tested for the continental and oceanic lithosphere of the European-North Atlantic region, where the predicted heat flow agrees with

high-quality conventional heat-flow measurements (Artemieva, 2019a). The method is fully independent and different in the approach, methodology, assumptions, and implementation from an earlier approach focused on crustal isostasy and crustal geotherms (Hasterok and Chapman, 2007).

Our calculations are constrained by analysis of the relationship between topography and Moho depth, and therefore the method is well suited for regions where Moho depth is known from seismic studies but with low density of heat-flow data and/or transient thermal regime, such as most of Tibet (Figure 2). By analyzing Airy-type correlation between topography and Moho depth (Figure 3), we separate crustal and mantle components to topography where the crustal component incorporates in situ crustal density variations associated with variable lithology and temperature.

The mantle component of the topography (termed here the anomalous topography) is assumed to originate only from lateral thermal variation (compositional heterogeneity plays a minor role, see analysis by Artemieva, 2019a). It constrains the thermal structure of the lithosphere with respect to a location where the anomalous topography is zero and where the lithosphere thermal thickness is known from independent data. The strength of the method is that it is free from an assumption on a steady-state equilibrium geotherm and therefore is well suited to study tectonically active regions (Artemieva, 2022), like Tibet and Himalayas, given that the Moho depth is well constrained. Another advantage of the method is that it constrains the present-day lithosphere thermal structure, in contrast to thermal modeling based on heat flow which reflects a past

thermal regime.

In the rest of this section (Subsections 5.2-5.4) we present a step-by-step explanation of the method together with the assumptions, which we discuss and test by the sensitivity analysis (subsection 5.5). We refer the reader to the original papers for further details of the method, sensitivity analysis, and comparison to actual heat-flow measurements (Artemieva, 2019a, b, 2022; Artemieva and Shulgin, 2019).

5.2 Crustal contribution to isostasy

The method assumes that (1) topography is maintained by isostatic contributions from the crust and the lithospheric mantle, and that (2) isostatic compensation is achieved at the lithosphere-asthenosphere boundary (LAB). Therefore, it is important that most of the region be close to isostatic equilibrium (Section 4.1). The results are poorly constrained for regions with strong deviations from isostatic equilibrium (much of Himalaya and the deformed margins of Tibet).

For Airy-type crustal isostasy, the slope of the linear correlation between Moho depth and topography (Figure 3a) constrains the in-situ density contrast across the Moho. Crustal and mantle densities both include compositional and thermal components, and we estimate crustal densities from linear correlation between topography and Moho Depth (Artemieva, 2019a, b, 2022). As some regions in our study area are out of equilibrium (i.e. have very large free-air anomalies, Figure 1c and 3b), we calculate the correlation between Moho depth and topography using only areas with free air gravity anomalies < ±80 mGal (Figure 3c). This choice yields a reference Moho depth of 36 km (Moho depth at zero topography defined

by the best-fit line in Figure 3a) and a slope of 5.24 km/km (Figure 3a).

The slope is controlled by the in-situ density contrast between the crust and the mantle, and the two densities cannot be uniquely determined from the slope. For geophysically plausible values, the slope of 5.24 km/km allows average in-situ crustal densities between 2.70 × 10^3 and 2.80 × 10^3 kg/m^3 and average in-situ mantle densities between 3.22 × 10^3 and 3.37 × 10^3 kg/m^3 (Fig. 5 in Artemieva and Shulgin, 2019). We adopt a reference crustal in-situ density of 2.75 × 10^3 kg/m^3, which yields 2.78 × 10^3 kg/m^3 at STP condition (i.e. at standard (room) temperature and pressure, T=20 °C, P=1 atm). To fit the slope value of 5.24 km/km (Figure 3a), we use an in-situ reference density of lithospheric mantle of 3.27 × 10^3 kg/m^3, corresponding to 3.38 × 10^3 kg/m^3 at STP condition (i.e. to reworked cratonic or Phanerozoic fertile mantle; Poudjom Djomani et al., 2001). Our conversion of in-situ to SPT densities assumes a temperature of 600 °C at the Moho and 1300 °C at the LAB, and a coefficient of thermal expansion of 3.5 x 10^{-5} K^{-1}. The choice of the reference density values has little effect on the results (Artemieva, 2019a,b), which instead depend on the density contrast across the Moho (the slope of the best-fit line in Airy-type crustal isostasy, Figure 3). We analyse uncertainties arising from the choice of reference crustal and mantle densities by sensitivity analysis in Section 5.5, Table 3, and Supporting Figures S4-S8.

5.3 Lithospheric mantle contribution to isostasy

If isostatic equilibrium were achieved at the Moho, the data in Figure 3 would plot around the best-fit line. Since this is not the case, there should also be a mantle contribution to isostasy, which justifies our assumption that isostasy is achieved at

the LAB. To estimate the contribution of the lithospheric mantle to isostasy, we calculate anomalous topography (Figure 4) as the deviation of the actual elevation (ETOPO1, Figure 1a) from the isostatically-predicted elevation (the best-fit line between the Moho depth and elevation, Figure 3). Therefore, anomalous topography reflects deviations from crustal isostasy (with the compensation depth at the Moho) and shows the presence of anomalous density masses between the Moho and the LAB (where isostatic equilibrium is achieved). Cold and dense sub-Moho material suppresses the topography, leading to negative anomalous topography values, and low-density (hot) sub-Moho material has the opposite effect.

In most of Tibet, the anomalous topography is weakly negative (- 0.4 ± 0.9 km and around -1 km in the Lhasa Block), suggesting the presence of cold and thick lithosphere. There are also areas with positive anomalous topography, so that the regional average for the entire study region is close to zero (-0.1 ± 1.1 km) (Figure 4).

The eastern Songpan-Ganzi Block, most of the Eastern Kunlun-Qaidam Block, the entire Qilian Block, and the adjacent part of the North China Craton have anomalous topography in the range of ± 1 km and close to zero on average. The Yangtze craton, the entire Lhasa Block, and most of the Qiangtang Block, except for its central part, have negative anomalous topography of -1.5 to 0 km; similar values are typical of the Tarim craton where the Moho depth is known.

One of the strongest positive topography anomalies of +2 to +3 km is observed in western Songpan-Ganzi and some parts of the Qiangtang and Qaidam-Eastern

Kunlun Blocks, suggesting the presence of an anomalously buoyant mantle. However, we note that the Eastern Kunlun Block is in disequilibrium (Fig. 1c). In the Himalayan belt, which is not in isostatic equilibrium and where the model therefore is poorly constrained, the anomalous elevation is typically -2 to +2 km, but locally reaches -4 to +3 km.

5.4 Lithosphere thermal structure

We next assume that all regional deviations of topography from crustal isostasy predictions (anomalous topography) are caused by (1) variation in lithospheric mantle thickness and (2) in-situ density anomalies in the lithospheric mantle, and that (3) mantle density anomalies are caused only by thermal expansion due to lithosphere thermal anomalies. Sensitivity analysis (Artemieva, 2019a, b) demonstrates that compositional variation in the lithospheric mantle can be ignored within model uncertainty. While removal of a possible dynamic contribution to topography from the mantle (Melosh and Raefsky, 1980) requires additional assumptions (Artemieva and Shulgin, 2019) and its effect is minor for areas with near-zero free-air anomalies, short wavelength lithosphere flexural deformation (Sandwell and Schubert, 1982) is effectively excluded by using spatial data averaging, which works as a low pass filter of the topography and Moho depth data (Supporting Figure S3).The role of lithosphere deformation (Sandwell and Schubert, 1982) is difficult to quantify, and we expect that it may be important in those parts of the region that deviate from isostatic equilibrium (Figure 1c) and where the results are poorly constrained.

Under these assumptions, anomalous topography can be used to infer lithospheric temperature anomalies (averaged over the entire lithospheric column) relative to locations with zero anomalous topography. Therefore, the calculation procedure requires *a priori* information on lithosphere thickness in a selected location with zero anomalous topography, which is used as a reference value for the calculations of lithosphere thickness anomalies for the entire region and for conversion of the LAB depth anomalies to absolute values (Figure 5a). We present results for a reference lithosphere thickness of 150 km (at locations with zero anomalous topography, Figure 4); the choice of other values will systematically shift the results (see Section 5.5 and Table 3 for sensitivity tests).

Thermal-lithosphere thickness is controlled by the lithospheric geotherm, which, in turn, correlates with surface heat flow (Pollack and Chapman, 1977; Pollack et al., 1993; Rudnick et al., 1998; Artemieva, 2006). This long-recognized global correlation allows us to predict heat-flow values, which can be tested against existing heat-flow data, where available. In our calculations of predicted surface heat flow, we adopt geotherms by Pollack and co-authors (1993) and limit our model to the lithospheric mantle. This way we avoid making any assumptions on the poorly known crustal heat production. For the European continent, the North Atlantic ocean and Greenland the method predicts heat-flow values in tight agreement with borehole measurements (Artemieva, 2019a,b).

5.5 Sensitivity analysis

The major uncertainty in our results originates from the uncertainty of the input parameters, including: i) Moho depth constrained by receiver function studies; ii)

density contrast across the Moho controlled by the slope of the best fit line in Figure 3a, and iii) reference lithosphere thickness in areas with zero anomalous topography (Figure 4) which is assumed to be known from independent data. Here we analyze the uncertainty of our results by calculating the dependence of the calculated lithosphere thermal thickness and predicted heat flow on the various input parameters. We present results of the sensitivity tests as values averaged for the entire study region shown in Figure 1 (Table 3) and in a series of maps (Supporting Figures S4-S8).

i) We present two tests for the effect of Moho depth: (a) for local and (b) for systematic regional Moho depth uncertainty. (a) For a location with an average regional elevation of ~2.7 km, corresponding to an average regional Moho depth of 52 km (Figure 3a), a change in local Moho depth by ±3 km will change anomalous topography by ca. 0.3 km. This will result in a change of lithosphere thickness by ca. ±30 km (19%) and a change of predicted surface heat flow by ±8 mW/m^2 (<16%). (b) If the reference value of the Moho depth (i.e. Moho depth at zero topography) is increased by 2 km (a regional systematic shift in the reference Moho depth, purple line in Figure 3a), the calculated lithosphere thickness decreases by 10-30 km (for the whole study region by 13 km on average) with an average increase in the predicted heat flow by 5 mW/m^2 (Supporting Figure S7 and Table 3).

ii) We expect regional variation in the density contrast across the Moho due to variation in the bulk composition of the crust (Wang et al., 2021) and the lithospheric mantle (Xia et al., 2020). The slope of the best-fit line between

topography and Moho depth (Figure 3a), which links the average in-situ densities of the crust and the lithospheric mantle, determines the calculated anomalous topography and, thereby, controls the lithosphere thermal model.

We test the case with an increase in reference crustal density (which controls the slope of the best-fit line in Figure 3a) from 2.75 × 10^3 kg/m^3 to 2.85 × 10^3 kg/m^3 (Table 3). Maintaining the best-fit slope of 5.24 km/km (black line in Figure 3a) leads to a change in in-situ mantle density from 3.27 × 10^3 kg/m^3 to an unrealistic in-situ value of 3.39 × 10^3 kg/m^3. We, therefore, keep the reference mantle density unchanged by changing the slope of the Moho depth-topography relation to 6.79 km/km and adjusting the reference Moho depth to 30 km; the latter choice ensures that the crustal isostasy Moho-topography line still crosses through most of the data points (blue dotted line in Figure 3a, test results in Supporting Figure S4). We also test the effects of reducing the reference crustal density to 2.70 × 10^3 kg/m^3 where we, similarly, adjust the reference Moho depth to 40 km (red dotted line in Figure 3a, test results in Supporting Figure S5). Finally, we test the effect of reducing the in-situ reference mantle density to 3.20 × 10^3 kg/m^3 where we adjust the reference crustal density to 2.80 ×10^3 kg/m^3 in order to maintain a realistic topography-Moho depth relation (turquoise dotted line in Figure 3a, test results in Supporting Figure S6). These tests correspond to laterally variable changes in the in-situ average crustal and/or average mantle densities and we calculate the anomalous topography, LAB depth and heat flow throughout the whole study area for different fixed lines relating Moho depth and topography for the three cases (Figure 3a).

The test for an increase in reference crustal density (Supporting Figure S4) leads to changes in anomalous topography with opposite signs in high- and low-elevation areas, leading to changes in the predicted LAB depth and heat flow with opposite signs throughout the region. Therefore, regionally averaged values of the LAB depth and heat flow remain largely unchanged as compared to our main results (Table 3), while local variations typically are within +/-20 km for the LAB depth and +/-5 mW/m^2 for heat flow. In the two other tests (Supporting Figures S5-S6), changes in anomalous topography have the same sign everywhere with an asymmetric effect in high- and low-elevation areas. Therefore, in both tests, the resultant changes in the LAB depth and the predicted heat flow are also asymmetric in high- and low-elevation areas and within 10% on average, with locally higher and smaller values (Table 3).

iii) The calculation procedure requires *a priori* information on lithosphere thickness at a reference location where the anomalous topography is zero (Figure 4). We adopt a reference lithosphere thickness of 150 km. The choice of a different value will systematically shift the results for lithosphere thermal thickness without changing the general pattern. A change (increase or decrease) of the reference value by 50 km will cause a corresponding change (increase or decrease) of the lithosphere thermal thickness by 20-40 km (on average 26%) and a change of predicted surface heat flow by ~5-10 mW/m^2 (on average 20%) (Supporting Figure S8 and Table 3).

6 Major patterns of lithosphere thermal thickness and heat flow variations

Our results show that Tibet has a strongly heterogeneous lithospheric structure at both long and short wavelengths (Figure 5a). High-quality surface heat-flow measurements are practically absent in Tibet from the Himalayan front to the Kunlun fault (Figures 1 and S1). However, heat flow predicted by our regional thermal model is in good agreement with the surface heat-flow measurements where they exist, as also found in regions with very good dense coverage of high-quality heat-flow measurements (Artemieva, 2019a). The predicted surface heat flow differs from the few available borehole measurements on average by 5.5 mW/m^2 ± 15.1 mW/m^2 (Figure 5b), that is within the expected accuracy (uncertainty) of the regional heat flow data (section 4.2). For example, in the Qaidam Block of NE Tibet, where the thermal-lithosphere thickness varies from 120 to 200 km, our model predicts a heat flow of 40-60 mW/m^2, so that the difference between the calculated and measured surface heat flow is 2.2 ± 19.1 mW/m^2.

Based on our lithosphere thermal model (Figure 5), we subdivide the region into several distinct domains (Figure 6):

1) The Lhasa Block has the thickest thermal lithosphere (>200 km thick) and a low surface heat flow of ca. 30-50 mW/m^2 (Figure 5). Such cold and thick lithosphere is typical of Archean cratons (Artemieva, 2006). However, there is only fragmentary evidence for the presence of Precambrian basement in the Lhasa terrane (Guynn et al., 2006) and, alternatively, we interpret that this thick thermal lithosphere is caused by the underthrusting of the Indian plate, which may have

placed cratonic lithosphere beneath this part of Tibet and “refrigerated” the lithosphere of the Lhasa Block. Our conclusion is along the lines of an earlier study of post-collisional magmatism in Tibet at 26-10 Ma in the Lhasa Block, which is interpreted to be caused by removal of pre-existing lithosphere at ~26 Ma, followed by underthrusting of the Indian lithosphere below southern Tibet (Chung et al., 2005).

2) In central-eastern Tibet south of the Kunlun fault (centered around 97° E/33° N), the thermal lithosphere is very thick (>200 km) with a surface heat flow of <50 mW/m^2, similar to the Lhasa Block (Figure 5). Since this domain cuts across the Bangong–Nujiang and Jinsha River sutures, this thick lithosphere may be associated with Tethyan paleo-slabs. Alternatively, it may mark a far northern extent of the underthrusting Indian plate, as previously suggested based on high Pn velocity (Liang & Song, 2006).

3) In northern Tibet (the western part of the Qiangtang and Songpan-Ganzi Blocks, in the area centered around 88° E/35° N), the lithosphere is very thin (<80 km) with inferred heat flow larger than 80-100 mW/m^2 (Figure 5). This region roughly corresponds to a zone of low Pn-velocity (Li and Song, 2018; McNamara et al., 1997) and inefficient Sn propagation (Ni & Barazangi, 1983) (Figure 7). The extent of this “North Tibet Anomaly” (Figure 6) cannot be well constrained due to the lack of seismic data on Moho depth (Figure 2a), such that information is available only at the margins of the anomalous area.

4) The Eastern Kunlun-Qaidam and Qilian Blocks of north-eastern Tibet, which represent Paleozoic orogenic belts, have a strongly heterogeneous

lithosphere thermal structure with a thickness of 100–150 km on average and predicted surface heat flow of 60 – 80 mW/m^2 (Figure 5). Small-scale anomalies with local thinning of the lithosphere to the Moho and heat flow locally exceeding 100 mW/m^2 are also observed in the eastern Songpan-Ganzi Block and central Himalaya. They are likely to be due to lithospheric deformation and local non-equilibrium conditions in regions where free-air gravity anomalies exceed ±80 mGal (Figure 1c). Alternatively, they may be caused by local short-wavelength variations in the density contrast across the Moho, most likely caused by crustal density anomalies, e.g. associated with mafic intrusions and underplating.

5) Stable blocks surrounding Tibet (the Tarim and Yangtze Cratons) have, in general, a thick cratonic-type thermal lithosphere, whereas the lithosphere of the western North China Craton is significantly thinner and warmer (Figures 5-7). Thick (200–240 km) lithosphere with low surface heat flow (40–45 mW/m^2), in close agreement with borehole data (with an average difference of -2.7 ± 10.0 mW/m^2; Figure 8), is present below the margins of the Tarim Craton where seismic data exists. A similar lithosphere thermal structure is predicted for the north-western part of the Yangtze Craton. However, in this area heat flow measurements from petroleum wells (Jiang et al., 2019) are systematically higher than our predictions (with an average difference of 7.8 ± 11.8 mW/m^2; Figure 8), possibly due to a systematic bias of measurements in boreholes with a non-equilibrated heat flow.

Likewise, there is some discrepancy (of 13.5 ± 10.5 mW/m^2 on average) in the predicted and measured heat flow in the western North China Craton. The largest difference (at around 108° E/35° N) is associated with the Cenozoic Weihe Graben.

In other parts of the western North China Craton our results predict surface heat flow around 45 mW/m^2 in the westernmost part and 60-70 mW/m^2 further eastwards, where the predicted and measured heat flow agree within the model and data uncertainties (Figures 5b, 8). Our results indicate that the lithosphere of the western North China Craton is only 120-180 km thick. East of 105^o E, where heat-flow data exist, the predicted values of 120-140 km are in overall agreement with the lithosphere thermal thickness based on surface heat flow (Xia et al., 2020), which constrains values of 90-140 km.

6) In general, topography is supported by the entire lithospheric column, including the crust and the upper mantle, although dynamic contributions from the mantle (Lithgow-Bertelloni and Silver, 1998) and lithosphere flexure (Watts, 2001) may also contribute to topography. For Tibet there is a clear linear correlation between topography and the fraction of crust in the lithosphere column (Figure 9), and other orogens are consistent with this trend. Blocks with the highest topography (the western parts of Qiangtang (W-QT) and Songpan-Ganzi (W-SGB), west of the North Tibet Anomaly, and Eastern Kunlun-Qaidam (W-EK) Blocks) have the largest fraction of the crust in the lithosphere column, 38-46% (Table 4). In contrast, the crustal fraction is only 25-30% in low-elevation regions of the Qaidam Block (QDB) and of the eastern parts of Qilian (E-QB) and Songpan-Ganzi (E-SGB) (east of the North Tibet Anomaly) Blocks. In the North Tibet Anomaly, the lithosphere may be thinned almost to the Moho, and so we exclude this anomalous region from the analysis (in Table 4 and Figure 9).

The two regions furthest from the general Tibetan trend line have some of the

thickest (>200 km) thermal lithosphere: the Lhasa Block (LB) and the eastern Qiangtang Block (E-QT) have the same high topography (>4.5 km, on average) as the western Qiangtang Block (W-QT), but the crustal fraction is only 33-34%, and not 42% as the Tibetan linear trend predicts. Note that the Alps also have a smaller fraction of crustal contribution than the trend prediction (Figure 9). A large contribution of lithospheric mantle to topography may be a characteristic feature of regions with thick lithosphere created by subducting slabs, as in the Lhasa Block and the Alps. This observation supports our interpretation that thick lithosphere beneath eastern Qiangtang Block (centered around 97° E/33° N) may correspond to the northern extent of the underthrusting Indian plate.

7 Heterogeneous thermal lithosphere of Tibet

7.1 The northern limit of the Indian plate

A part of the heterogeneous thermal structure of the Tibetan lithosphere (Figures 5) may reflect fragmentation of the underthrusting Indian plate, which may remain intact beneath the cold, thick lithosphere of the Lhasa Block and the eastern and western parts of the Qiangtang Block. The northern limit of the Indian plate may be controlled by variations in the dip angle and slab tearing. In our interpretation it may be marked by the northern extent of thick lithosphere, shown by colored line in Figure 6.

In the western part of Tibet (~78-84° E), the northern limit of the thick thermal lithosphere crudely follows the Jinsha River suture (~34-36° N). The thick lithosphere may represent the sub-horizontal or gently dipping Indian plate

extending up to almost ~36-38° N at ~74-77° E, where it adjoins the south-western edge of the Tarim Craton (Kufner et al., 2016; Zhao et al., 2010).

In the central section of Tibet (~84-94° E), the front of the Indian plate may be located at around 32-34° N at around the Bangong-Nujiang suture (Figure 6). This location is similar to an earlier proposed lithosphere discontinuity at 31° N at 85°E (Nabelek et al., 2009).

Further east (~ 94-100° E), the thick thermal lithosphere may extend further north of the Jinsha River suture to ~ 35-36° N. The eastern extent of the thick lithosphere block is not marked by any prominent faults or sutures. Instead, the "Eastern Tibet" block with thick lithosphere crosses two major suture zones, the Bangong–Nujiang and Jinsha River sutures.

In contrast, the Longmenshan fault is marked by a sharp change in the lithosphere thickness of ca. 50 km. It separates a relatively thin (80-120 km) lithosphere of the Songpan-Ganzi Block from the thick lithosphere of the Yangtze Craton, suggesting that it is a lithosphere-scale fault.

7.2 Hot mantle of the North Tibet Anomaly

A remarkable feature of our results is the sharp decrease in lithosphere thermal thickness from >180 km to <80 km in central Tibet (~84-92° E/~33-38° N), across the Bangong–Nujiang suture (Figures 5a, 6). As previously mentioned, the exact size of the anomaly cannot be resolved due to the absence of data on the crustal thickness in this area. Note that most of the existing geophysical profiles also do not constrain the size of the anomalous area, and image its margins only (Figure 1b).

The North Tibet Anomaly area (the north-central Qiangtang and central Songpan-Ganzi Blocks) has an extremely thin lithosphere (<80 km and possibly thinned to the Moho, such that lithospheric mantle is basically absent) and high predicted heat flow (>90 mW/m^2). These observations are consistent with seismic evidence for a low Pn velocity (Li and Song, 2018; McNamara et al., 1997) and inefficient Sn propagation (Ni and Barazangi, 1983) reported for the southern margin of the anomalous area (Figure 1b), as well as Plio-Pleistocene volcanic activity (Guo and Wilson, 2019). Crustal xenoliths from this area also indicate high lower-crustal temperature of >800-1000 °C (Ding et al., 2007; Hacker et al., 2000; Wang et al., 2016).

We interpret the North Tibet Anomaly as the junction of two subduction systems with opposite polarities: the northward Indian subduction and the southward Tarim (Asian) subduction. The interplay of two subducting systems may have created slab windows and asthenosphere upwelling as inferred from geochemical data (Guo and Wilson, 2019), and may have created a thin and hot lithosphere as inferred from our modeling results.

8 Conclusions

We constrain the thermal lithosphere in Tibet and adjacent regions using the thermal isostasy method (Artemieva, 2019a, b; Artemieva and Shulgin, 2019) based on our compilation of seismic Moho depth in the region. We demonstrate that the lithospheric thermal structure of Tibet is highly heterogeneous, likely due to lateral variations in the northern extent of Indian subduction, the southward

subduction of the Asian plate, and possible preservation of fragmented Tethyan paleo-slabs.

- In most of the Lhasa Block, the thickness of the thermal lithosphere exceeds 200 km and surface heat flow is low, 40–45 mW/m^2. A block with a similar cratonic thermal structure is also present in eastern Tibet (beneath the eastern segment of the Qiangtang and Songpan-Ganzi Blocks at ~96-98^o E). Thick thermal lithosphere in southern and eastern Tibet is likely to represent on-going underthrusting of the Indian lithosphere; its northern limit may mark the longitudinally variable northern extent of the Indian plate to 33–36^o N. Alternatively, in eastern Tibet, where thick lithosphere is observed beneath the Bangong–Nujiang and Jinsha River sutures, it may be associated with Tethyan paleo-slabs. In far-western Tibet (74-78^o E), the thick lithosphere continues northwards to the margin of the Tarim Craton.
- We identify the North Tibet Anomaly (~84-92° E/~33-38° N) south of the Altyn-Tag fault in the central Qiangtang and Songpan-Ganzi Blocks. In this North Tibet Anomaly zone, the lithosphere is very thin (<80 km) and surface heat flow is very high (>90 mW/m^2) in a region with inefficient seismic Sn propagation and low Pn velocity. The anomaly may be caused by lithosphere delamination and asthenospheric upwelling in the area between the northernmost extent of the northward subducting Indian plate and the southernmost extent of the southward subducting the Asian plate.
- The Tarim Craton, where data on the Moho depth are available, and the north-western part of the Yangtze Craton have typical cold and thick (200-240 km)

cratonic lithosphere, whereas the lithosphere thickness is 120-180 km in western North China Craton. In the Qaidam deep sedimentary basin the lithosphere is 100-120 km thick.

- The strongly heterogeneous lithospheric thermal structure in Tibet and the surrounding blocks suggests that an interplay of several mechanisms maintains the high elevation of Tibet.

Acknowledgements:

The authors acknowledge the following research grants: BX - National Science Foundation of China Grant 41904090; BX, IMA and HT - National Science Foundation of China Grant 92055210 to HT; IMA - Inge Lehmann Grant of the Royal Danish Academy of Sciences and Letters; HT - Large grant DFF/FNU-16/059776-15 of the Danish Fund for Independent Research; SLK - US NSF Grant EAR1628282. BX thanks Xiao-Bo Tian, Xiao-Feng Liang and Yun Chen for discussions. Comments and suggestions from D. Hasterok and anonymous reviewers are acknowledged.

Declaration of competing interest:

The authors declare no conflict of interest.

Data Availability Statement

Data used in calculations are available at Zenodo:

https://doi.org/10.5281/zenodo.5930767.

References

Artemieva, I.M., 2006. Global 1°×1° thermal model TC1 for the continental lithosphere: Implications for lithosphere secular evolution. Tectonophysics 416, 245–277. doi:10.1016/j.tecto.2005.11.022.

Artemieva, I.M., 2019a. Lithosphere structure in Europe from thermal isostasy. Earth-Science Reviews, 188, 454-468. doi:10.1016/j.earscirev.2018.11. 004.

Artemieva, I.M., 2019b. Lithosphere thermal thickness and geothermal heat flux in Greenland from a new thermal isostasy method. Earth-Science Reviews, 188, 469-481. doi:10.1016/j.earscirev.2018.10.015.

Artemieva, I.M., 2022. Antarctica ice sheet basal melting enhanced by high mantle heat. Earth-Science Reviews, 226, 103954. doi: 10.1016/j.earscirev.2022.103954.

Artemieva, I., Thybo, H., Shulgin, A., 2016. Geophysical constraints on geodynamic processes at convergent margins: A global perspective. Gondwana Research 33, 4–23. doi:10.1016/j.gr.2015.06.010.

Artemieva, I.M., Shulgin, A., 2019. Geodynamics of Anatolia: Lithosphere Thermal Structure and Thickness. Tectonics 38, 4465–4487. doi:10.1029/2019tc005594.

Chan, G.N., Waters, D., Searle, M., et al., 2009. Probing the basement of southern Tibet: evidence from crustal xenoliths entrained in a Miocene ultrapotassic dyke. Journal of the Geological Society 166, 45–52. doi:10.1144/0016-76492007-145.

Chen, S.W., Wang, B.S., Tian, X.F., et al., 2016. Crustal structure from Yunxian-Ninglang wide-angle seismic reflection and refraction profile in northwestern Yunnan, China. Seismology and Geology 38, 91–106 (in Chinese).

Chen, Y., Li, W., Yuan, X.H., Badal, J., Teng, J.W., 2015. Tearing of the Indian lithospheric slab beneath southern Tibet revealed by SKS-wave splitting measurements. Earth and Planetary Science Letters 413, 13–24. doi:10.1016/j.epsl.2014.12.041.

Chung, S.-L., Chu, M.-F., Zhang, Y., et al., 2005. Tibetan tectonic evolution inferred from spatial and temporal variations in post-collisional magmatism. Earth-Science Reviews, 68, 173-196.

Craig, T.J., Kelemen, P.B., Hacker, B.R. and Copley, A., 2020. Reconciling geophysical and petrological estimates of the thermal structure of Southern Tibet. Geochemistry, Geophysics, Geosystems, 21(8), p.e2019GC008837. doi: 10.1029/2019GC008837

Cui, Z.Z., Lu, D.Y., Chen, J.P., et al., 1987. The deep structure and tectonic features of the crust in Panxi area. Acta Geophysica Sinica 30, 566–580 (in Chinese).

Ding, L., Kapp, P., Yue, Y., Lai, Q., 2007. Postcollisional calc-alkaline lavas and xenoliths from the southern Qiangtang terrane, central Tibet. Earth and Planetary Science Letters 254, 28–38. doi:10.1016/j.epsl.2006.11.019.

England, P., Houseman, G., 1988 . The mechanics of the Tibetan Plateau. Philosophical Transactions of the Royal Society of London. Series A, Mathematical and Physical

Sciences 326, 301–319. doi: 10.1098/rsta.1988.0089.

Francheteau, J., Jaupart, C., Jie, S.X., et al., 1984. High heat flow in southern Tibet. Nature 307, 32–36.doi:10.1038/307032a0.

Galvé, A., Hirn, A., Jiang, M., et al., 2002. Modes of raising northeastern Tibet probed by explosion seismology. Earth and Planetary Science Letters 203, 35–43. doi:10.1016/S0012-821X(02)00863-4.

Galvé, A., Jiang, M., Hirn, A., et al., 2006. Explosion seismic P and S velocity and attenuation constraints on the lower crust of the North–Central Tibetan Plateau, and comparison with the Tethyan Himalayas: Implications on composition, mineralogy, temperature, and tectonic evolution. Tectonophysics 412, 141–157. doi:10.1016/j.tecto.2005.09.010.

Ge, R., Zhu, W., Wilde, S. A., Wu, H., 2018. Remnants of Eoarchean continental crust derived from a subducted proto-arc. Science Advances 4, eaao3159. doi: 10.1126/sciadv.aao3159

Guo, Z., Wilson, M., 2019. Late Oligocene–early Miocene transformation of post-collisional magmatism in Tibet. Geology 47, 776–780. doi:10.1130/G46147.1.

Guynn, J.H., Kapp, P., Pullen, A., et al., 2006. Tibetan basement rocks near amdo reveal "missing" mesozoic tectonism along the bangong suture, central tibet. Geology 34, 505. doi:10.1130/g22453.1.

Hacker, B.R., Gnos, E., Ratschbacher, L., 2000. Hot and Dry Deep Crustal Xenoliths from Tibet. Science 287,2463–2466. doi:10.1126/science.287.5462.2463.

Hasterok, D., Chapman, D.S., 2007. Continental thermal isostasy: 1. Methods and sensitivity. Journal of Geophysical Research 112 B06414. doi: 10.1029/2006JB004663

Hou, Z.Q., Gao, Y.F., Qu, X.M., et al., 2004. Origin of adakitic intrusives generated during mid-Miocene east–west extension in southern Tibet. Earth and Planetary Science Letters 220, 139–155. doi:10.1016/s0012-821x(04)00007-x.

Hu, H.X., Lu, H.X., Wang, C.Y., et al., 1986. Explosion investigation of the crustal structure in western Yunnan Province. Acta Geophysica Sinca 29, 133–144 (in Chinese).

Institute of Geophysics and Academia Sinica, 1981. Explosion seismic study for velocity distribution and structure of the crust and upper mantle from Danxung to Yasong of Xizang Plateau. Acta Geophysica Sinica 24, 155–170.

Jaupart, C., Mareschal, J.C., 2011. Heat Generation and Transport in the Earth. Cambridge University Press. pp464 doi:10.1017/CBO9780511781

Jia, S.X., Guo, W.B., Mooney, W.D., et al., 2019. Crustal structure of the middle segment of the Qilian fold belt and the coupling mechanism of its associated basin and range system. Tectonophysics 770, 128–154. doi:10.1016/j.tecto.2019.06.024.

Jia, S.X., Liu, B.J., Xu, Z.F., et al., 2014. The crustal structures of the central Longmenshan along and its margins as related to the seismotectonics of the 2008 Wenchuan Earthquake. Science China Earth Sciences 57, 777–790. doi:10.1007/s11430-013-4744-9.

Jiang, G.Z., Hu, S.B., Shi, Y.Z., et al., 2019. Terrestrial heat flow of continental China:

Updated dataset and tectonic implications. Tectonophysics 753, 36–48. doi:10.1016/j.tecto.2019.01.006.

Jiang, M., Galvé, A., Hirn, A., et al., 2006. Crustal thickening and variations in architecture from the Qaidam basin to the Qang Tang (North–Central Tibetan Plateau) from wide-angle reflection seismology. Tectonophysics 412, 121–140. doi:10.1016/j.tecto.2005.09.011.

Jiménez-Munt, I., Fernàndez, M., Vergés, J., Platt, J.P., 2008. Lithosphere structure underneath the Tibetan Plateau inferred from elevation, gravity and geoid anomalies. Earth and Planetary Science Letters 267, 276–289. doi:10.1016/j.epsl.2007.11.045.

Karplus, M.S., Zhao, W., Klemperer, S.L., et al., 2011. Injection of Tibetan crust beneath the south Qaidam Basin: Evidence from INDEPTH IV wide-angle seismic data. Journal of Geophysical Research 116. doi:10.1029/2010jb007911.

Klemperer, S.L., 2006. Crustal flow in Tibet: geophysical evidence for the physical state of Tibetan lithosphere, and inferred patterns of active flow. Geological Society of London. 268, 39-70. doi:10.1144/GSL.SP.2006.268.01.03.

Kufner, S.K., Schurr, B., Sippl, C., et al., 2016. Deep India meets deep Asia: Lithospheric indentation, delamination and break-off under Pamir and Hindu Kush (central Asia). Earth and Planetary Science Letters 435, 171–184. doi:10.1016/j.epsl.2015.11.046.

Li, J.T., Song, X.D., 2018. Tearing of Indian mantle lithosphere from high-resolution seismic images and its implications for lithosphere coupling in southern Tibet. Proc. Nat. Acad. Sci. 115, 8296–8300. doi:10.1073/pnas.1717258115.

Li, Q.H., Guo, J.K., Zhou, M.D., Wei, D.Q., Fan, B., Hou, X.Y., 1991. The crustal velocity structure of Chengxian-Xiji profile. Northwestern Seismological Journal 13, 37–43 (in Chinese).

Li, Q.S., Peng, S.P., Gao, R., Fan, J.Y., 2003. Seismic evidence of the basement uplift in the Bayan Har tectonic belt, Qinghai and its tectonic significance. Geological Bulletin of China 22, 782–788 (in Chinese).

Li, S.L., Zhang, X.K., Zhang, C.K., Zhao, J.R., Cheng, S.X., 2002. A preliminary study on the crustal velocity structure of Maqin-Lanzhou-Jingbian by means of deep seismic sounding profile. Chinese Journal of Geophysics 45, 210–217 (in Chinese).

Li, W.H., Gao, R., Wang, H.Y., et al., 2017. Crustal structure beneath the Liupanshan fault zone and adjacent regions. Chinese Journal of Geophysics 60, 2265–2278. doi:10.6038/cjg20170619.

Li, Y.K., Gao, R., Gao, J.W., et al., 2015. Characteristics of crustal velocity structure along Qingling oroginic belt. Progress in Geophysics 30, 1056–1069. doi:10.6038/pg20150309.

Liang, X.F., Sandvol, E., Chen, Y.J., et al., 2012. A complex Tibetan upper mantle: A fragmented Indian slab and no south-verging subduction of Eurasian lithosphere. Earth Planet. Sci. Letters 333-334, 101–111. doi:10.1016/j.epsl.2012.03.036.

Liu, C.Z., Wu, F.Y., Chung, S.L., Zhao, Z.D., 2011. Fragments of hot and metasomatized mantle lithosphere in Middle Miocene ultrapotassic lavas, southern Tibet. Geology 39, 923–926. doi:10.1130/g32172.1.

Liu, H.B., Teng, J.W., Yin, Z.X., 1990. Characteristics of the 2-D crustal structure and fault

distribution beneath the Seilin Co Yangamdo in the Northern Xizang Plateau. Bulletin of the Chinese Academy of Geological Sciences 21, 259–267 (in Chinese).

Liu, M.J., Mooney, W.D., Li, S.L., Okaya, N., Detweiler, S., 2006. Crustal structure of the northeastern margin of the Tibetan plateau from the Songpan-Ganzi terrane to the Ordos basin. Tectonophysics 420, 253–266. doi:10.1016/j.tecto.2006.01.025.

Lithgow-Bertelloni, C. , Silver, P. 1998. Dynamic topography, plate driving forces and the African superswell. Nature, 395, 269–272.

Lu, D.Y., Wang, X.J., 1990. The crustal structure and deep internal processes in the Tuotuohe-Golmuc area of the north Qinghai-Xizang Plateau. Bulletin of the Chinese academy of geologgical sciences 21, 227–237 (in Chinese).

Makarov, V.I., Alekseev, D.V., Batalev, et al., 2010. Underthrusting of Tarim beneath the Tien Shan and deep structure of their junction zone: Main results of seismic experiment along MANAS Profile Kashgar-Song-Köl. Geotectonics 44, 102–126. doi:10.1134/s0016852110020020.

McKenzie, D. P., Priestley, K. F. 2008. The influence of lithospheric thickness variations on continental evolution. Lithos, 102, 1-11. doi: 10.1016/j.lithos.2007.05.005

McNamara, D.E., Walter, W.R., Owens, T.J., Ammon, C.J., 1997. Upper mantle velocity structure beneath the Tibetan Plateau from Pn travel time tomography. Journal of Geophysical Research: Solid Earth 102, 493–505. doi:10.1029/96JB02112.

Mechie, J., Sobolev, S., Ratschbacher, L., et al., 2004. Precise temperature estimation in the Tibetan crust from seismic detection of the α-β quartz transition. Geology 32, 601. doi:10.1130/G20367.1.

Mechie, J., Zhao, W.J., Karplus, M.S., et al., 2012. Crustal shear (S) velocity and Poisson's ratio structure along the INDEPTH IV profile in northeast Tibet as derived from wide-angle seismic data. Geophysical Journal International 191, 369–384. doi:10.1111/j.1365-246x.2012.05616.x.

Melosh, H.J., Raefsky, A., 1980. The dynamical origin of subduction zone topography. Geophysical Journal International 60, 333–354. doi:10.1111/j.1365-246x. 1980.tb04812.x.

Min, X.Y., Zhou, M.D., Guo, J.K., et al., 1991. The crustal velocity structure in Lingtai-Amuquhu profile. Northwestern Seismological Journal 13, 29–36 (in Chinese).

Murodov, D., Zhao, J.M., Xu, Q., et al., 2018. Complex N–S variations in Moho depth and Vp/Vs ratio beneath the western Tibetan Plateau as revealed by receiver function analysis, Geophysical Journal International, 214, 895–906, doi:10.1093/gji/ggy170

Nabelek, J., Hetenyi, G., Vergne, J., et al., 2009. Underplating in the Himalaya-Tibet Collision Zone Revealed by the Hi-CLIMB Experiment. Science 325, 1371–1374. doi:10.1126/science.1167719.

Ni, J., Barazangi, M., 1983. High-frequency seismic wave propagation beneath the Indian Shield, Himalayan Arc, Tibetan Plateau and surrounding regions: high uppermost mantle velocities and efficient Sn propagation beneath Tibet. Geophysical Journal International 72, 665–689. doi:10.1111/j.1365-246X.1983.tb02826.x.

Pavlis, N.K., Holmes, S.A., Kenyon, S.C., Factor, J.K., 2012. The development and

evaluation of the Earth Gravitational Model 2008 (EGM2008). Journal of Geophysical Research: Solid Earth 117. doi:10.1029/2011JB008916.

Poudjom Djomani, Y.H.P., O'Reilly, S.Y., Griffin, W., Morgan, P., 2001. The density structure of subcontinental lithosphere through time. Earth and Planetary Science Letters 184, 605–621. doi:10.1016/s0012-821x(00)00362-9.

Pollack, H. N., Chapman, D. S. 1977. On the regional variation of heat flow, geotherms and the thickness of the lithosphere. Tectonophys. 38, 279–296. doi: 10.1016/0040-1951(77)90215-3

Pollack, H. N., Hurter, S. J., Johnson, J. R., 1993. Heat flow from the Earth's interior: analysis of the global data set. Rev. Geophys. 31, 267–280. doi: 10.1029/93RG01249

Roger, F., Jolivet, M., Malavieille, J., 2010. The tectonic evolution of the Songpan-Garzê (North Tibet) and adjacent areas from Proterozoic to Present: A synthesis. Journal of Asian Earth Sciences 39, 254–269. doi:10.1016/j.jseaes.2010.03.008.

Rudnick, L. R., McDonough, W. F., O'Connel, R. J., 1998. Thermal structure, thickness and composition of continental lithosphere. Chem. Geol. 145, 395–411. doi: 10.1016/S0009-2541(97)00151-4

Sandwell, D., Schubert, G., 1982. Lithospheric flexure at fracture zones. Journal of Geophysical Research: Solid Earth 87, 4657–4667. doi:10.1029/jb087ib06p04657.

Shi, D., Klemperer, S.L., Shi, J., Wu, Z., Zhao, W., 2020). Localized Foundering of Indian Lower Crust in the India-Tibet Collision Zone. Proceedings of the National Academy of Sciences 117, 24742-24747. doi: 10.1073/pnas.2000015117

Tapponnier, P., Xu, Z.Q., Roger, F., et al., 2001. Oblique Stepwise Rise and Growth of the Tibet Plateau. Science 294, 1671–1677. doi:10.1126/science.105978.

Teng, J.W., Li, S.L., Zhang, Y.Q., et al., 2014. Fine velocity structures and deep processes in crust and mantle of the Qinling orogenic belt and the adjacent North China craton and Yangtze craton. Chinese Journal of Geophysics 57, 3154–3175. doi:10.6038/cjg20141006.

Teng, J.W., Sun, K.Z., Xiong, S.B., et al., 1983a. Deep seismic reflection waves and structure of the crust from Dangxung to Yadong on the Xizang Plateau (Tibet). Physics of the Earth and Planetary Interiors 31, 293–306. doi:10.1016/0031-9201(83)90089-4 (in Chinese).

Teng, J.W., Xiong, S.B., Yin, Z.X., et al., 1983b. Structure of the crust and upper mantle pattern and velocity distributional characteristics at northern region of the Himalayan mountains. Acta Geophysica Sinca 26, 525–540 (in Chinese).

Tilmann, F., 2003. Seismic Imaging of the Downwelling Indian Lithosphere Beneath Central Tibet. Science 300, 1424–1427. doi:10.1126/science.1082777.

Unsworth, M., Wenbo, W., Jones, A.G., et al., 2004. Crustal and upper mantle structure of northern Tibet imaged with magnetotelluric data. Journal of Geophysical Research: Solid Earth 109. B02403 doi:10.1029/2002JB002305.

Vozar, J., Jones, A.G., Fullea, J., et al., 2014. Integrated geophysical-petrological modeling of lithosphere-asthenosphere boundary in central Tibet using electromagnetic and seismic data. Geochemistry, Geophysics, Geosystems 15, 3965–3988. doi:10.1002/2014GC005365.

Wang, C.y., Chen, W. P., Wang, L. O., 2013. Temperature beneath Tibet, Earth and Planetary Science Letters, 375, 326-337, doi: 10.1016/j.epsl.2013.05.052.

Wang, C.Y., Han, W.B., Wu, J.P., Lou, H., Chan, W.W., 2007. Crustal structure beneath the eastern margin of the Tibetan Plateau and its tectonic implications. Journal of Geophysical Research 112, B07307. doi:10.1029/2005JB003873.

Wang, G. C, Thybo, H., Artemieva, I.M., 2021. No mafic layer in 80 km thick Tibetan crust. Nature Communications doi: 10.1038/s41467-021-21420-z.

Wang, Q., Hawkesworth, C.J., Wyman, D., et al., 2016. Pliocene Quaternary crustal melting in central and northern Tibet and insights into crustal flow. Nature Communications 7. doi:10.1038/ncomms11888.

Wang, S.J., Liu, B.J., Zhang J.S, Liu, B.F., et al., 2015a. Study on the velocity structure of the crust in Southwest Yunnan of the north-south seismic belt—Results from the Menghai-Gengma-Lushui deep seismic sounding profile. Science China: Earth Sciences 58, 2175–2187. doi:10.1007/s11430-015-5189-0.

Wang, S.J., Wang, F.Y., Zhang, J.S., et al., 2015b. The deep seismogenic environment of Lushan Ms7.0 earthquake zone revealed by a wide-angle reflection/refraction seismic profile. Chinese Journal of Geophysics 58, 3193–3204. doi:10.6038/cjg20150915 (in Chinese).

Wang, S.J., Liu, B.J., Tian, X.F., et al., 2018. Crustal P-wave velocity structure in the northeastern margin of the Qinghai-Tibetan Plateau and insights into crustal deformation. Science China Earth Sciences 61, 1221–1237. doi:10.1007/s11430-017-9227-7.

Wang, S.Q., Klemperer, S.L., 2021. Love-wave normal modes discriminate between upper-mantle and crustal earthquakes: Simulation and demonstration in Tibet. Earth and Planetary Science Letters 571, 117089. doi: 10.1016/j.epsl.2021.117089

Wang, Y.X., Mooney, W.D., Huan, G.H., et al., 2005. Crustal P-wave velocity structure from Altyn Tagh to Longmen mountains along the Taiwan-Altay geoscience transect. Chinese Journal of Geophysics 48, 98–106 (in Chinese).

Wang, Y.X., Mooney, W.D., Yuan, X.C., Okaya, N., 2013. Crustal Structure of the Northeastern Tibetan Plateau from the Southern Tarim Basin to the Sichuan Basin, China. Tectonophysics 584, 191–208. doi:10.1016/j.tecto.2012.09.003.

Watts, A. B. 2001. Isostasy and Flexure of the Lithosphere. Cambridge University Press, 458 pp.

Wei, W.B., Unsworth, M., Jones, A., et al., 2001. Detection of Widespread Fluids in the Tibetan Crust by Magnetotelluric Studies. Science 292, 716–719. doi:10.1126/science.1010580.

Xia, B., Thybo, H., Artemieva, I.M., 2020. Lithosphere mantle density of the North China Craton. Journal of Geophysical Research: Solid Earth 125. e2020JB020296. doi:10.1029/2020jb020296.

Xiong, S.B., Liu, H.B., 1997. Crustal structure in western Tibetan plateau. Chinese Science Bulletin 42, 665–669 (in Chinese).

Xiong, S.B., Zheng, Y., Yin, Z.X., et al., 1993. The 2-D structure and it's tectonic implications of the crust in the Lijiang-Panzhihua-Zhehai region. Acta Geophysica

Sinics 36, 434–444 (in Chinese).

Xu, T., Zhang, Z.J., Liu, B.F., et al., 2015. Crustal velocity structure in the Emeishan large igneous province and evidence of the Permian mantle plume activity. Seicence China Earth Sciences 45, 561–576. Doi:10.1007/s11430-015-5094-6.

Yin, A., Harrison, T.M., 2000. Geologic Evolution of the Himalayan-Tibetan Orogen. Ann. Rev. Earth Planet. Sci. 28, 211–280. doi:10.1146/annurev.earth.28.1.211.

Yin, Z.X., Xiong, S.B., 1992. Explosion seismic study for the 2-D crustal structure in Xichang-Sukou-Muding Region. Acta Geophysica Sinica 35, 451–458 (in Chinese).

Zhang, J.S., Wang, F.Y., Liu, B.F., et al., 2014. A study of the crust-manlte velocity structure beneath the Yushu earthquake zone and its adjacent areas. Seismology and Geology, 36, 322-332

Zhang, S.Q., Wu, L.J., Guo, J.M., et al., 1985. An interpretation of the DSS data on Menyuan-Pingling-Weinan profile in west China. Acta Geophysica Sinica 28, 460–472 (in Chinese).

Zhang, X.K., Jia, S.X., Zhao, J.R., et al., 2008. Crustal structures beneath West Qinling-East Kunlun orogen and its adjacent area-results of wide-angle seismic reflection and regraction experiment. Chinese Journal of Geophysics 51, 439–450 (in Chinese).

Zhang, X.Y., Gao, R., Bai, Z.M., Xu, T., Li, Q.S., 2017. Crustal structure beneath the Longmenshan area in eastern Tibet: new constraints from reprocessing wide-angle seismic data of the Aba-Longmenshan-Suining profile. Chinese Journal of Geophysics 60, 2200–2212. doi:10.6038/dig20170614 (in Chinese).

Zhang, Z., Xu, C.M., Meng, B.Z., Liu, C., Teng, J.W., 2007. Crustal reflectivity characters from the Eryuan-Jiangchuan wide-angle seismic profile. Chinese Journal of Geophysics 50, 1082–1088 (in Chinese).

Zhang, Z., Zhao, B., Zhang, X., Liu, C., 2006. Crustal structure beneath the wide-angle seismic profile between Simao and Zhongdian in Yunnan. Chinese Journal of Geophysics 49, 1377–1384 (in Chinese).

Zhang, Z.J., Bai, Z.M., Klemperer, S., et al., 2013. Crustal structure across northeastern Tibet from wide-angle seismic profiling: Constraints on the Caledonian Qilian orogeny and its reactivation. Tectonophysics 606, 140–159. doi:10.1016/j.tecto.2013.02.040.

Zhang, Z.J., Bai, Z.M., Mooney, W., et al., 2009. Crustal structure across the Three Gorges area of the Yangtze platform, central China, from seismic refraction/wide-angle reflection data. Tectonophysics 475, 423–437. doi:10.1016/j.tecto.2009.05.022.

Zhang, Z.J., Bai, Z.M., Wang, C.Y., et al., 2005a. Crustal structure of Gondwana- and Yangtze-type blocks: An example by wide-angle seismic profile from Menglian to Malong in western Yun-nan. Science in China Series D-Earth Sciences 48, 1828–1836. doi:10.1360/03yd0547.

Zhang, Z.J., Bai, Z.M., Wang, C.Y., et al., 2005b. The crustal structure under Sanjiang and its dynamic implications: Revealed by seismic reflection/refraction profile between Zhefang and Binchuan, Yunnan. Science in China Series D-Earth Sciences 48, 1329–1336. doi:10.1360/01yd0567.

Zhang, Z.J., Deng, Y.F., Teng, J.W., et al., 2011. An overview of the crustal structure of the Tibetan plateau after 35 years of deep seismic soundings. Journal of Asian Earth Sciences 40, 977–989. doi:10.1016/j.jseaes.2010.03.010.

Zhang, Z.J., Klemperer, S., 2010. Crustal structure of the Tethyan Himalaya, southern Tibet: new constraints from old wide-angle seismic data. Geophysical Journal International 181, 1247–1260. doi:10.1111/j.1365-246X.2010.04578.x.

Zhang, Z.J., Klemperer, S., Bai, Z.M., Chen, Y., Teng, J.W., 2011. Crustal structure of the Paleozoic Kunlun orogeny from an active-source seismic profile between Moba and Guide in East Tibet, China. Gondwana Research 19, 994–1007. doi:10.1016/j.gr.2010.09.008.

Zhang, Z.J., Li, Y.K., Wang, G.J., et al., 2001. East-west crustal structure and "down-bowing" Moho under the northern Tibet revealed by wide-angle seismic profile. Science in China (Series D) 31, 881–888.

Zhang, Z.J., Teng, J.W., Li, Y.K., Klemperer, S., Yang, L.Q., 2002. Crustal structure of seismic velocity in southern Tibet and east-westward escape of the crustal material—An example by wide-angle seismic profile from Peigu Tso to Pumoyong Tso. Science in China (Series D) 32, 793–798. doi:10.1360/zd2002-32-10-793.

Zhao, J.M., Jin, Z.J., Mooney, W.D., et al., 2013. Crustal structure of the central Qaidam basin imaged by seismic wide-angle reflection/refraction profiling. Tectonophysics 584, 174–190. doi:10.1016/j.tecto.2012.09.005.

Zhao, J.M., Mooney, W.D., Zhang, X.K., et al., 2006. Crustal structure across the Altyn Tagh Range at the northern margin of the Tibetan Plateau and tectonic implications. Earth and Planetary Science Letters 241, 804–814. doi:10.1016/j.epsl.2005.11.003.

Zhao, J.M., Yuan, X.H., Liu, H.B., et al., 2010. The boundary between the Indian and Asian tectonic plates below Tibet. Proceedings of the National Academy of Sciences 107, 11229–11233. doi:10.1073/pnas.1001921107.

Zhao, W.J., Kumar, P., Mechie, J., et al., 2011. Tibetan plate overriding the Asian plate in central and northern Tibet. Nature Geoscience 4, 870–873. doi:10.1038/ngeo1309.

Zhu, D.C., Zhao, Z.D., Niu, Y., et al., 2013. The origin and pre-Cenozoic evolution of the Tibetan Plateau. Gondwana Research 23, 1429–1454. doi:10.1016/j.gr.2012.02.002.

Chardon, D., Jayananda, M., Chetty, T. R. K., and Peucat, J.-J. (2008), Precambrian continental strain and shear zone patterns: South Indian case, J. Geophys. Res., 113, B08402, doi:10.1029/2007JB005299

Liang, C., & Song, X. (2006). A low velocity belt beneath northern and eastern Tibetan Plateau from Pn tomography. Geophysical Research Letters, 33, L22306. https://doi.org/10.1029/2006GL027926

Styron, R., Taylor, M., & Okoronkwo, K. (2010). HimaTibetMap-1.0: New 'web-2.0' online database of active structures from the Indo-Asian collision. Eos, 91(20), 181. https://doi.org/10.1029/2010EO200001

Figure captions

Figure 1: (a) Topography and simplified tectonics of Tibet and adjacent regions. Geological boundaries after Styron et al. (2010). Purple and yellow lines mark sutures from closure of Paleo-Tethys and Neo-Tethys, respectably; black lines are strike-slip faults (bold if slip > 8 mm/year); thin red lines are normal and thrust faults. Abbreviations: AKMS: Anyemaqen suture, ATF: Altyn Tagh fault; BNS: Bangong–Nujiang suture, IYS: Indus–Yarlung suture, JS: Jinsha River suture, KLF: Kunlun fault, LMF: Longmenshan trust fault, NQF: North Qinling fault. **(b)** Lithosphere thermal observations from previous studies. Colored circles – high-quality surface heat-flow measurements (Jiang et al., 2019). Red, green and blue lines – inferred thin, normal and thick lithosphere based on geophysical observations (numbers 1-12, see Table 1 for details and references); red ellipse (number 1) – region with low Pn velocity and inefficient Sn propagation (Ni and Barazangi, 1983; McNamara et al., 1997); stars (numbers 13-16, cf. Table 1) – xenolith-based thermal studies. **(c)** Simplified free-air gravity anomalies at sea level from EGM-2008 (Pavlis et al., 2012) and major tectonic blocks. Shaded areas with high values of the anomalies are poorly constrained by the present study.

Figure 2: Crustal-scale seismic studies of Tibet and adjacent regions (See Table 2 for references). **(a)** Receiver functions (yellow dots) and seismic wide-angle reflection/refraction profiles (blue lines: recorded prior to 2000; green lines: 2000-2010; red lines: after 2010; dark gray: INDEPTH profiles). **(b)** Moho

depth based on receiver function (RF) results. **(c)** Moho depth based on seismic wide-angle reflection/refraction profiles. **(d)** Difference in Moho depth between receiver-function studies and wide-angle reflection/refraction studies.

Figure 3: Moho depth versus topography for the whole region shown in Figure 2; data are sampled on a 0.25° x 0.25° grid to filter out uncompensated short wavelength deformation. **(a)** Data density with the parameters determined for Airy-type crustal isostasy (only data points with free air gravity anomalies of < ± 80 mGal are used). Best fit line (thick, black) is: [Moho depth in km] = 36.0 km + 5.24* [Topography in km]; blue, red, cyan and purple lines are different reference models used for sensitivity analyses presented in section 5.5 and Table 3. **(b)** All data points color-coded by free-air gravity; **(c)** Data points with free-air gravity of < ± 80 mGal. Plots (b) and (c) have the same color scale as Figure 1c.

Figure 4: Anomalous topography: positive values represent isostatically-predicted topography higher than actual topography, indicating the presence of a buoyant, low-density sub-Moho material; and vice-versa. Hatching – areas where the results are poorly constrained.

Figure 5: (a) Thermal-lithosphere thickness calculated by thermal isostasy; **(b)** Calculated surface heat flow overlain by measured values (colored dots); the

color scales for predicted and measured heat flow are the same. Hatching – areas where the results are poorly constrained.

Figure 6: Simplified sketch map of lithospheric thermal structure based on Figure 5. Thick color lines are our interpretations of the front of the subducted India lithosphere and the edge of the southward Tarim subduction.

Figure 7: Lithospheric cross-sections based on receiver-functions for the Moho depth and on our results for thermal-lithosphere thickness (LAB depth). Abbreviations for faults and sutures are as in Figure 1a. Insert shows locations of the cross-sections with abbreviated names of tectonic blocks. Profiles 2 and 4 cross the North Tibet Anomaly (Figure 6) with inefficient Sn propagation and low Pn velocity (Li and Song, 2018; McNamara et al., 1997; Ni and Barazangi, 1983). LM: lithospheric mantle; AM: Asthenospheric mantle.

Figure 8: Histogram of the difference between measured and predicted surface heat flow for various tectonic blocks. For most of the region, in particular within Tibet, predicted and measured values are statistically similar. Predicted values are statistically slightly smaller than measured values in two stable blocks, which are western parts of the North China and Yangtze cratons. In the North China craton most of the discrepancy is along the southern edge at the border with the Qinling orogen.

Figure 9: Relative fraction of the crust in the lithosphere versus topography for various blocks in Tibet (see Table 4). Abbreviations: LB: Lhasa Block; QT: Qiangtang Block; SGB: Songpan Ganzi Block; QDB: Qaidam Block; EK: Eastern Kunlun Block; QB: Qilian Block; preceding E and W refer to eastern and western parts of tectonic blocks, respectively. For the Qiangtang and Songpan-Ganzi Blocks, the western and eastern parts are those parts outside the North Tibet Anomaly, which is excluded from the analysis because the lithosphere may be thinned almost to the Moho in this zone.

Table Captions

Table 1: Previous studies of thermal structure of Tibet

Table 2. Seismic studies on the Moho depth used in the study

Table 3: Sensitivity analyses for input parameters in the modeling

Table 4: Topography, depths to the Moho (Figure 2b) and to thermal LAB (Figure 5a), and relative fractional thickness of the crust in the total lithospheric column for different tectonic blocks of Tibet (the North Tibet Anomaly is excluded).

a) Topography

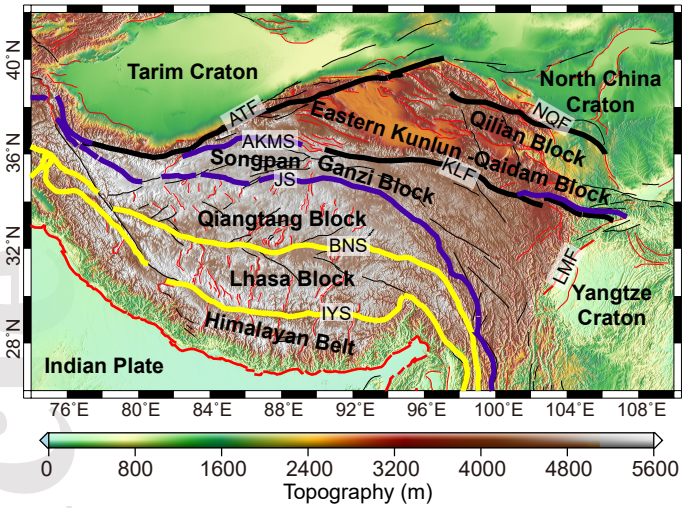

b) Lithosphere thermal state

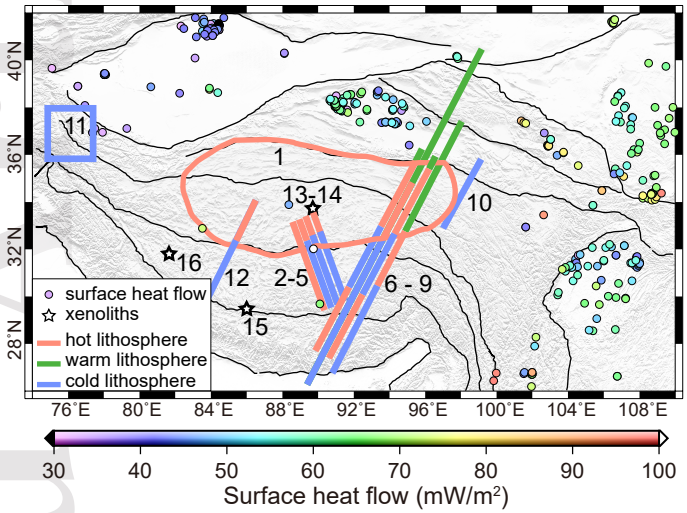

c) Simplified Free-air Gravity Anomaly

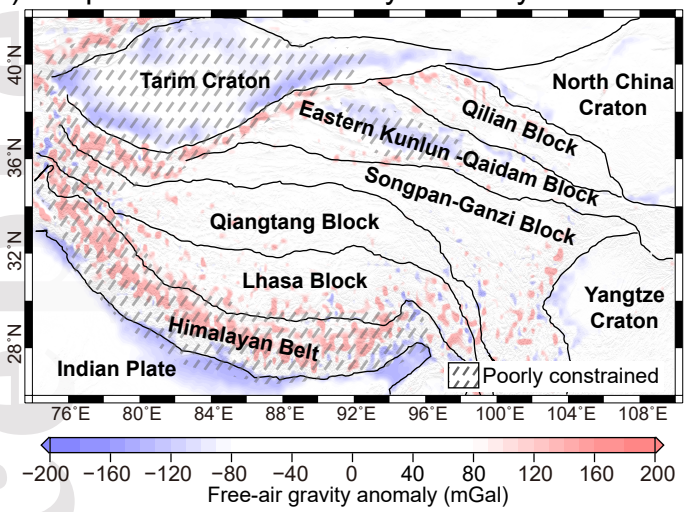

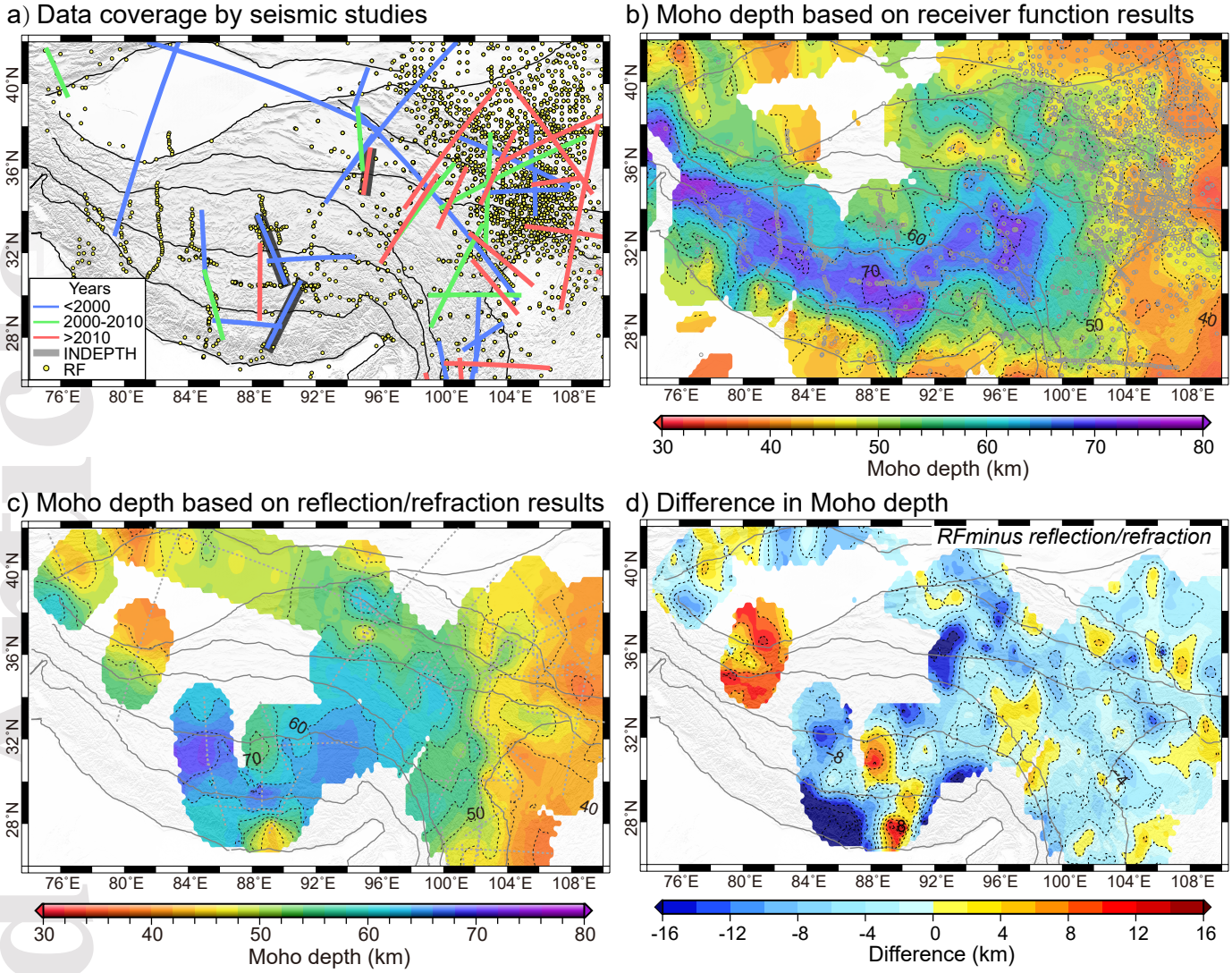

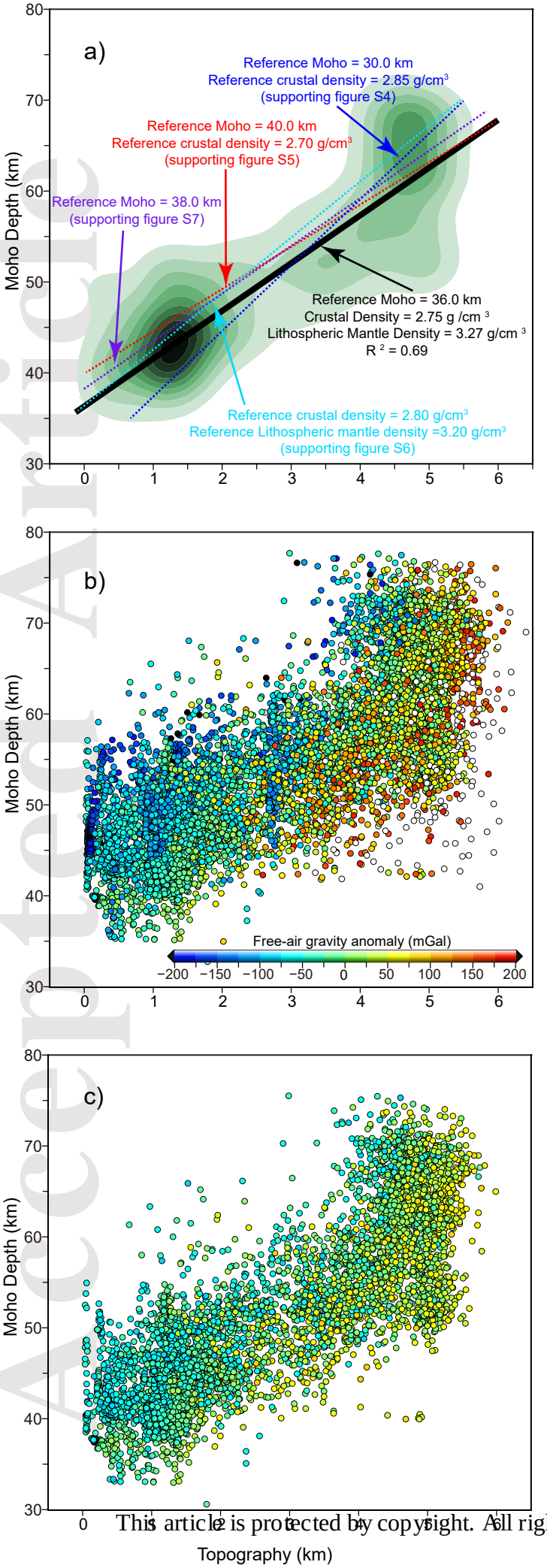

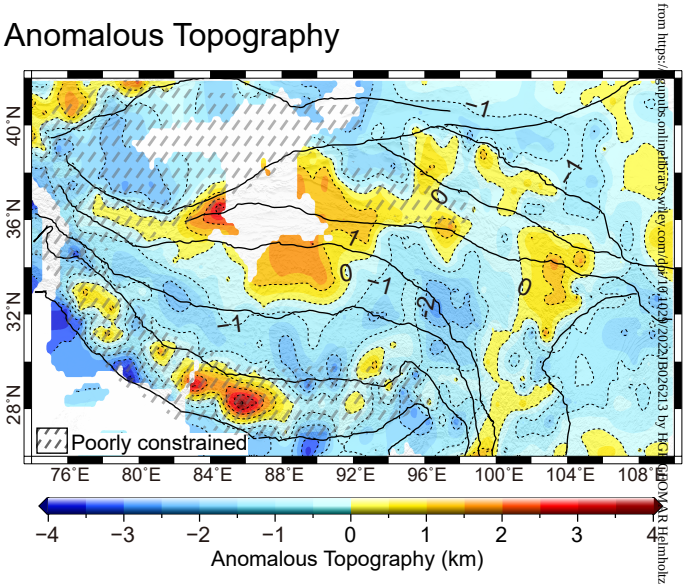

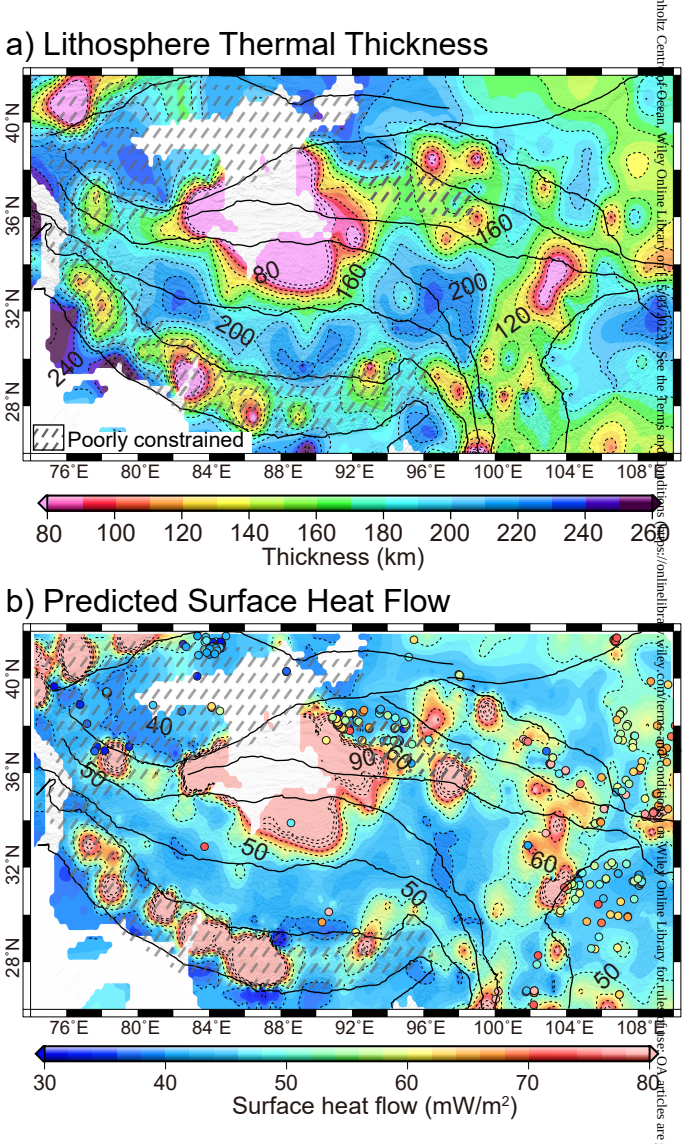

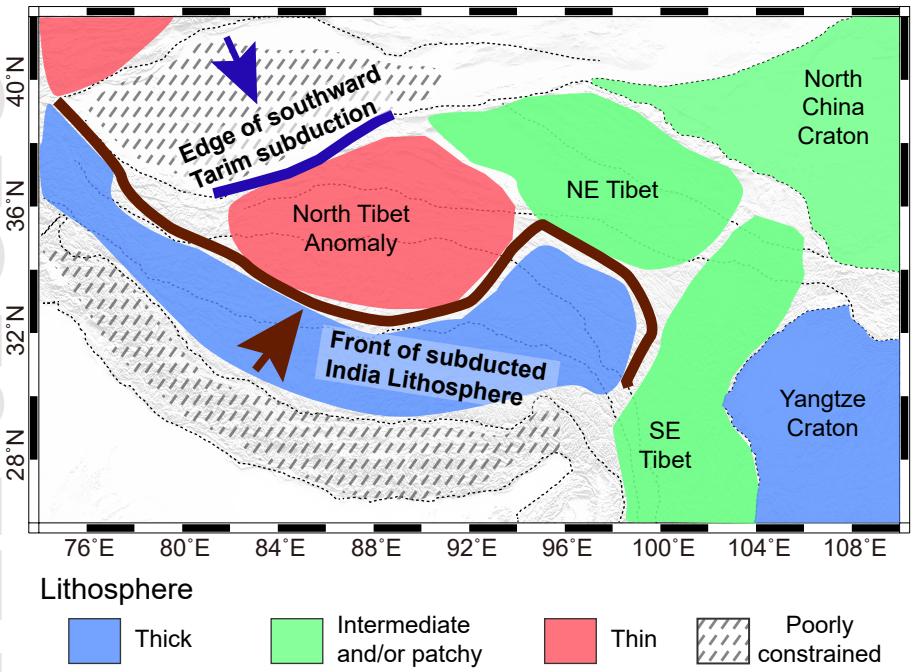

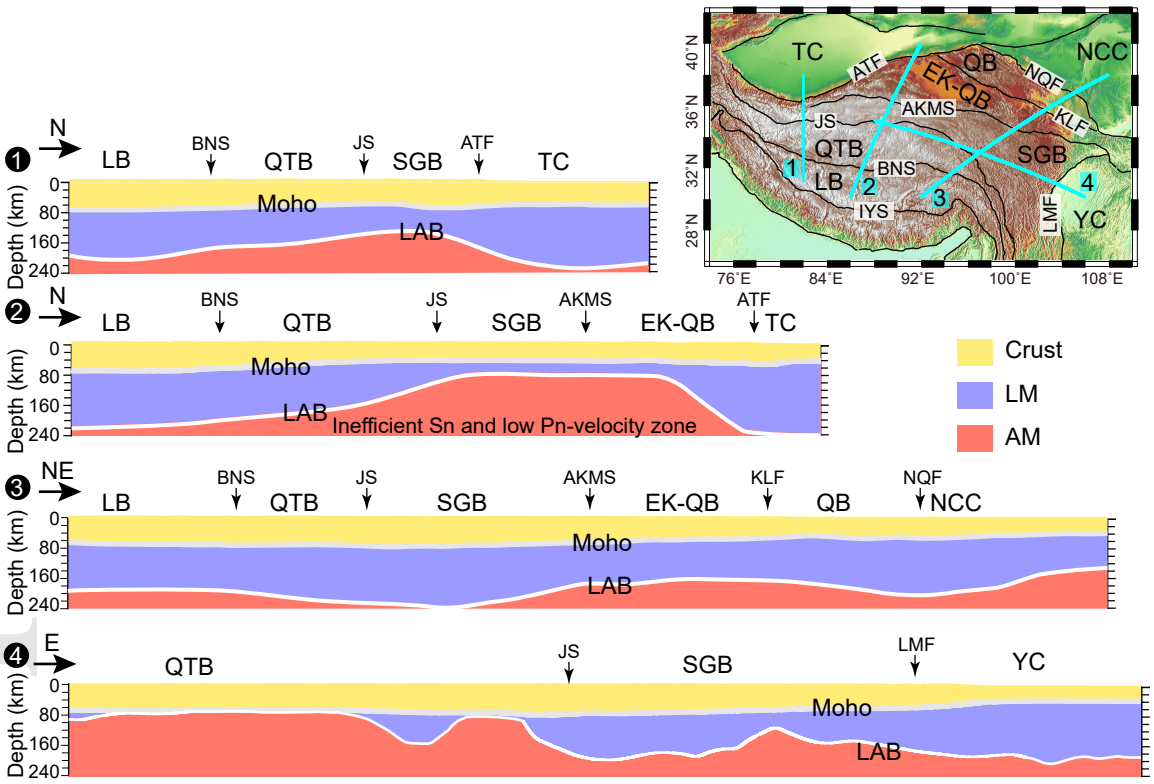

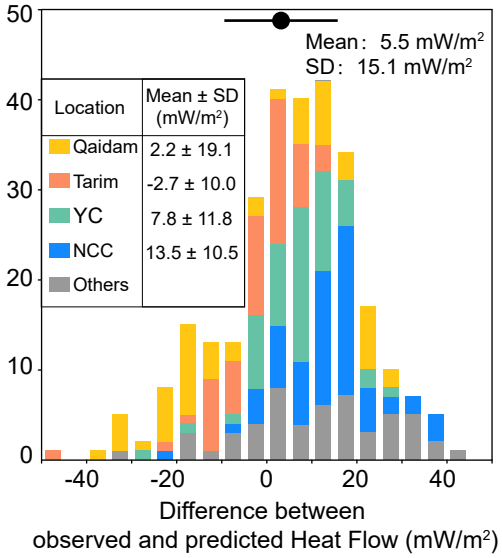

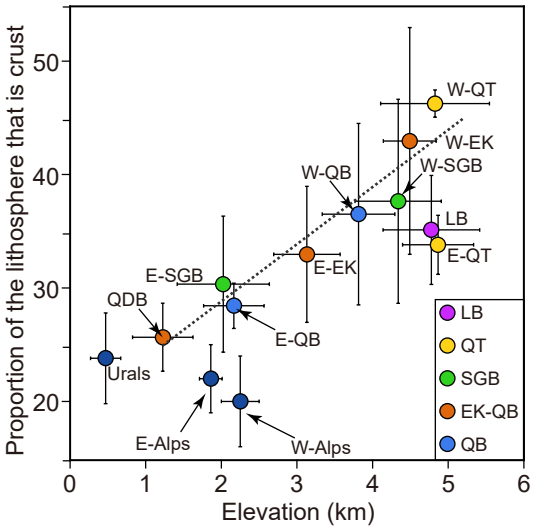

Table 1. Previous studies of thermal structure of Tibet

No. in Fig. 1b	Method	Reference
1	Pn and Sn results	McNamara et al., 1997; Ni and Barazangi, 1983
2	P-wave mantle tomography (INDEPTH III)	Tilmann et al., 2003
3	α-β quartz transformation (INDEPTH III)	Mechie et al., 2004
4	Crustal-scale integrated geophysical-petrological modeling (INDEPTH III)	Vozar et al., 2014
5	Earthquake thermometry (INDEPTH III)	Wang et al., 2013
6	P-wave mantle tomography	Liang et al., 2012
7	Gravity modeling	Jiménez-Munt et al., 2008
8	S-receiver function	Zhao et al., 2011
9	MT	Wei et al., 2001; Unsworth et al., 2004
10	Crustal Vp, Vs and Q	Galvé et al., 2005
11	upper-mantle earthquakes	Wang and Klemperer, 2021
12	thermal modeling	Craig et al., 2020
13-15	Crustal xenoliths	Hacker et al. 2000; Ding et al., 2007; Chan et al., 2009
16	Mantle xenoliths	Liu et al, 2011

Table 2. Seismic studies of the Moho depth used in the study

Receiver Function studies	Reference
Receiver Function Moho	Chen et al., 2015; He et al., 2014; Li et al., 2014; Murodov et al., 2018; Pan and Niu, 2011; Tian et al., 2015; Wang et al., 2017; Xu et al., 2018; Yue et al., 2012; Zhang et al., 2014; Zheng et al., 2015
Reflection/refraction profiles	Reference
INDEPTH_III	Mechie et al., 2012
INDEPTH_IV	Karplus et al., 2011
Yadong–Dangxiong	Institute of Geophysics and Academia Sinica, 1981; Teng et al., 1983a
Peigutso–Pumoyongtso	Teng et al., 1983b; Zhang et al., 2002; Zhang and Klemperer, 2010
Selintso–Yaanduo	Liu et al., 1990; Zhang et al. 2001
Cuoqin–Sangehu	Xiong and Liu, 1997
Cuoqin–Zhangmu	Zheng et al., 2004
LT-TH	Wang et al., 2021
Daichaidan-Baicheng	Zhao et al., 2006
Xiji-Zhongwei	Li et al., 2001
Lingtai-Amuquhu	Min et al., 1991
Menyuan-Weinan	Zhang et al., 1985
Chengxian-Xiji	Li et al., 1991
Altyn–Altai	Wang et al., 2005; Wang et al., 2013
Tuotuohe–Golmud	Lu and Wang, 1990; Li et al., 2003
Golmud–Ejinaqi	Cui et al., 1995
Maqin–Jingbian	Li et al., 2002; Liu et al., 2006
Yushu–Gonghe	Galve et al., 2002; Jiang et al., 2006
Markang–Gulang	Zhang et al., 2008
Moba-Guide	Zhang et al., 2011
Hezuo-Jingtai	Zhang et al., 2013
Geermu-Huahaizi	Zhao et al., 2013

Ordos-Liupanshan	Li et al., 2017
Nangqian-Huashixia	Zhang et al., 2014
Xigu-Yulin	Wang et al., 2018
Fuping-Alax	Wang et al., 2018
Chongqing-Yulin	Teng et al., 2014
Longnan-Shiyan	Li et al., 2015
Maduo-Yabulai	Jia et al., 2019
Zhubalong–Zizhong	Wang et al., 2007
Tangke–Benzilan	Wang et al., 2007
Aba-Suining	Jia et al., 2014; Zhang et al., 2017
Jinchuan-Leshan	Wang et al., 2015a
Lijiang–Zhehai	Xiong et al., 1993
Lijiang-Qingzhen	Xu et al., 2015
Zhongdian-Simao	Zhang et al., 2006
Zhefang-Binchuan	Hu et al., 1986; Zhang et al., 2005a
Menglian-Malong	Hu et al., 1986; Zhang et al., 2005b
Eryuan-Jiangchuan	Hu et al., 1986; Zhang et al., 2007
Changheba-Lazha	Cui et al., 1987
Lijiang-Xinzhen	Cui et al., 1987
Xichang-Mouding	Yin and Xiong, 1992
Dima-Lushui	Wang et al., 2015b
Yunxian-Ningliang	Chen et al., 2016
Three_Gorges	Zhang et al., 2009
MANAS	Makarov et al., 2010
Quanshuigou-Dushanzi	Li et al., 2001

Table 3. Sensitivity analysis of input parameters in the modeling

Input model parameter for the final results (Fig. 5a)				Modeling results averaged for the entire study region		
Reference crustal in situ density, kg/cm^3 (x 10^3)	Reference mantle in situ density, kg/cm^3 (x 10^3)	Reference Moho depth, km	Reference lithosphere thickness, km	Calculated lithosphere thermal thickness, km	Predicted heat flow, mW/m^2	
2.75*	3.27*	36**	150***	166	50****	
Tested reference parameters				Corresponding results (and change (in %) with respect to the final results)		Supporting figures
2.85		30		173 (+4%)	52 (-4%)	Figure S4
2.70		40		152 (-8%)	56 (+11%)	Figure S5
2.80	3.20			153 (-7%)	55 (+10%)	Figure S6
		38		153 (-7%)	55 (+10%)	Figure S7
			100	123 (-26%)	60 (+20%)	Figure S8

* Determined from the regional best-fit in Figure 3a for Airy-type isostasy, see section 5.2 for details.

** Moho depth at zero topography (Figure 3a)

*** Assumed for locations with AT=0 km in Fig. 4, see section 5.3 for details.

**** Method cannot constrain values >120 mW/m^2 (Artemieva, 2019b, 2022).

Table 4. Topography, depths to the Moho (Fig. 2b) and to thermal LAB (Fig. 5a), and relative fractional thickness of the crust in the total lithospheric column for different tectonic blocks of Tibet (the North Tibet Anomaly is excluded).

	Topography (km)		Moho depth (km)		LAB depth* (km)		Percent of crust (%)	
	Mean	σ	Mean	σ	Mean	σ	Mean	σ
Lhasa Block	4.78	0.64	65	6	189	29	35	5
W-Qiangtang Block	4.83	0.72	59	5	134	28	46	12
E-Qiangtang Block	4.87	0.47	66	3	198	17	34	3
W-Songpan-Ganzi Block	4.34	0.57	58	6	163	39	38	9
E-Songpan-Ganzi Block	2.03	0.61	48	4	163	23	30	6
Qaidam Block	1.22	0.40	43	4	172	33	26	3
W-Eastern Kunlun Block	4.49	0.35	53	3	129	29	43	10
E-Eastern Kunlun Block	3.13	0.44	52	5	162	32	33	6
W-Qinlian Block	3.81	0.48	54	3	154	29	37	8
E-Qinlian Block	2.17	0.40	49	4	172	18	28	3

E- eastern part; W- western part; the western and eastern parts of the Qiangtang and Songpan-Ganzi Blocks are respectively west of and east of the North Tibet Anomaly, which is not considered here.

* Lithosphere thermal thickness (LAB depth) is defined as the depth where the geotherm reaches a potential temperature of 1300 ºC.